Dual-Polarization Deconvolution and Geophysical Retrievals from the Advanced Microwave Precipitation Radiometer during OLYMPEX/RADEX

COREY G. AMIOT,[a] SAYAK K. BISWAS,[b] TIMOTHY J. LANG,[c] AND DAVID I. DUNCAN[d]

[a] *Department of Atmospheric and Earth Science, The University of Alabama in Huntsville, Huntsville, Alabama*
[b] *The Aerospace Corporation, El Segundo, California*
[c] *NASA Marshall Space Flight Center, Huntsville, Alabama*
[d] *European Centre for Medium-Range Weather Forecasts, Reading, United Kingdom*

(Manuscript received 22 December 2019, in final form 15 October 2020)

ABSTRACT: Recent upgrades, calibration, and scan-angle bias reductions to the Advanced Microwave Precipitation Radiometer (AMPR) have yielded physically realistic brightness temperatures (T_b) from the Olympic Mountains Experiment and Radar Definition Experiment (OLYMPEX/RADEX) dataset. Measured mixed-polarization T_b were converted to horizontally and vertically polarized T_b via dual-polarization deconvolution, and linear regression equations were developed to retrieve integrated cloud liquid water (CLW), water vapor (WV), and 10-m wind speed (WS) using simulated AMPR T_b and modeled atmospheric profiles. These equations were tested using AMPR T_b collected during four OLYMPEX/RADEX cases; the resulting geophysical values were compared with independent retrieval (1DVAR) results from the same dataset, while WV and WS were also compared with in situ data. Geophysical calculations using simulated T_b yielded relatively low retrieval and crosstalk errors when compared with modeled profiles; average CLW, WV, and WS root-mean-square deviations (RMSD) were 0.11 mm, 1.28 mm, and 1.11 m s^{-1}, respectively, with median absolute deviations (MedAD) of 2.26×10^{-2} mm, 0.22 mm, and 0.55 m s^{-1}, respectively. When applied to OLYMPEX/RADEX data, the new retrieval equations compared well with 1DVAR; CLW, WV, and WS RMSD were 9.95×10^{-2} mm, 2.00 mm, and 2.35 m s^{-1}, respectively, and MedAD were 2.88×10^{-2} mm, 1.14 mm, and 1.82 m s^{-1}, respectively. WV MedAD between the new equations and dropsondes were 2.10 and 1.80 mm at the time and location of minimum dropsonde altitude, respectively, while WS MedAD were 1.15 and 1.53 m s^{-1}, respectively, further indicating the utility of these equations.

KEYWORDS: Wind; Water vapor; Aircraft observations; Cloud retrieval; Microwave observations; Remote sensing

1. Introduction

a. Overview

The purpose of this manuscript is to summarize the dual-polarization upgrade of the National Aeronautics and Space Administration (NASA) Advanced Microwave Precipitation Radiometer (AMPR), provide details of geophysical retrievals that are possible with the upgraded AMPR system, and demonstrate these retrieval methods using data from NASA's Olympic Mountains Experiment (OLYMPEX) and Radar Definition Experiment (RADEX). OLYMPEX took place from fall 2015 to spring 2016 in collaboration with RADEX (Houze et al. 2017). The primary goal of OLYMPEX was to examine how precipitation is affected by flow over the Olympic Mountains of Washington in the United States, while RADEX focused on improving satellite-based retrievals of cloud and precipitation properties. Numerous instruments, including AMPR, were deployed to the study domain around northwestern Washington. AMPR, which flew on board a NASA Earth Research 2 (ER-2) high-altitude research aircraft during OLYMPEX/RADEX, is a cross-track scanning total power radiometer that operates at four radio-frequency channels with central frequencies at 10.7, 19.35, 37.1, and 85.5 GHz (Spencer et al. 1994). At the 20-km primary flight altitude for the ER-2 during OLYMPEX/RADEX, the 10.7 and 19.35 GHz frequencies have a footprint diameter of roughly 2.8 km, while the 37.1 and 85.5 GHz frequencies have footprint diameters of approximately 1.5 and 0.6 km, respectively. However, all AMPR data are sampled at the 85.5-GHz (0.6 km) channels' intervals in the along-scan (i.e., cross-track) direction (Spencer et al. 1994).

b. AMPR polarimetric upgrade and calibration

AMPR's antenna system consists of a dedicated feedhorn for the 10.7-GHz channel and a separate feedhorn for the higher-frequency channels. Both feedhorns have dual-orthogonal polarization outputs for each frequency channel. In past studies (e.g., Vivekanandan et al. 1993; Smith et al. 1994; Evans et al. 1995; McGaughey et al. 1996; Cecil et al. 2010), only one feedhorn polarization was measured using a single receiver for each channel. AMPR's two fixed feedhorns combined with cross-track scanning via a rotating mirror resulted in brightness temperature (T_b) scenes that were vertically polarized at one edge of the scan, horizontally polarized at the other edge, and mixed polarization for intermediate scan angles. With this configuration, it was not possible to unambiguously retrieve true horizontally and vertically polarized T_b across the entire AMPR scene. To account for this, a second receiver was added for each channel to measure the orthogonal

Supplemental information related to this paper is available at the Journals Online website: https://doi.org/10.1175/JTECH-D-19-0218.s1.

Corresponding author: Corey G. Amiot, ca0019@uah.edu

DOI: 10.1175/JTECH-D-19-0218.1

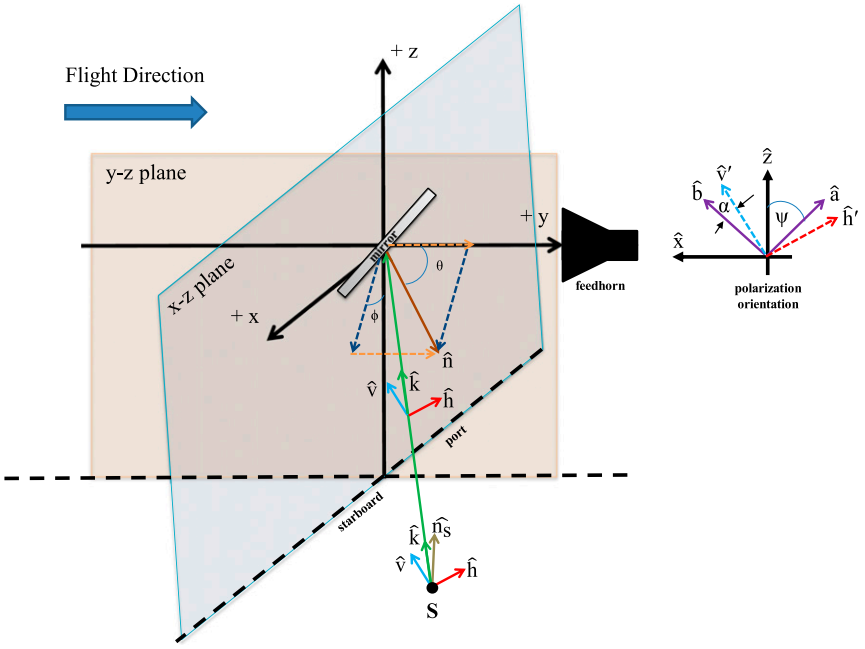

FIG. 1. Diagram illustrating the polarization mixing geometry present within the AMPR system during a typical flight. In this diagram, ϕ is the scan angle, θ is the reflector-normal angle, ψ is the polarization-rotation angle of the feedhorn, and $\alpha = \phi'$ is the polarization-basis-rotation angle; all other variables correspond to their respective vectors or angles as indicated within the diagram. Adapted from Biswas et al. (2017).

feedhorn polarization. This allowed for orthogonal mixed-polarization T_b values to be gathered across the entire AMPR scene, from which vertical- and horizontal-polarization T_b suitable for geophysical parameter retrievals can be estimated. Due to the fixed feedhorns and rotating mirror, AMPR scene polarization basis rotates with respect to the feedhorn polarization basis for each scan angle. A diagram presenting these system and scan properties can be found in Fig. 1.

Following Piepmeier et al. (2008), for a rotation angle ϕ', the relationship between T_b in the scene polarization basis and measured T_b in the feedhorn polarization basis is given by

$$\overline{\mathbf{T}_f} = \begin{pmatrix} T_{fA} \\ T_{fB} \\ T_{f3} \\ T_{f4} \end{pmatrix} = \begin{bmatrix} \sin^2(\phi') & \cos^2(\phi') & -\frac{1}{2}\sin(2\phi') & 0 \\ \cos^2(\phi') & \sin^2(\phi') & \frac{1}{2}\sin(2\phi') & 0 \\ \sin(2\phi') & -\sin(2\phi') & -\cos(2\phi') & 0 \\ 0 & 0 & 0 & 1 \end{bmatrix} \begin{pmatrix} T_v \\ T_h \\ T_3 \\ T_4 \end{pmatrix} = \overline{\overline{V(\phi')}} \cdot \overline{\mathbf{T}}, \tag{1}$$

where $\overline{\mathbf{T}_f}$ is the measured T_b vector at the feedhorn, $\overline{\mathbf{T}}$ is the true scene T_b vector, T_b subscripts v, h, 3, and 4 indicate vertically polarized, horizontally polarized, third stokes, and fourth stokes T_b, respectively, and nominally for AMPR $\phi' = \phi - 45°$, where ϕ is off-nadir scan angle. In Eq. (1), ϕ is measured positive (negative) toward the starboard (port) side of the observation platform. The 45° difference between ϕ' and ϕ is due to the AMPR feedhorn polarization axes being rotated 45° about the scan axis. From Eq. (1), exact estimation of T_v and T_h requires measurement of T_3, which is not presently measured in the AMPR system. For AMPR T_b scenes where the vertically and horizontally polarized signals are uncorrelated, Eq. (1) can be simplified to produce

$$\overline{\mathbf{T}_f} = \begin{pmatrix} T_{fA} \\ T_{fB} \end{pmatrix} = \begin{bmatrix} \sin^2(\phi') & \cos^2(\phi') \\ \cos^2(\phi') & \sin^2(\phi') \end{bmatrix} \begin{pmatrix} T_v \\ T_h \end{pmatrix} = \overline{\overline{u(\phi')}} \cdot \overline{\mathbf{T}}, \tag{2}$$

the reverse transformation of which is given by

$$\overline{\mathbf{T}} = \overline{\overline{u(-\phi')}} \cdot \overline{\mathbf{T}_f}, \tag{3}$$

which can be used to estimate true horizontally and vertically polarized T_b from the mixed-polarization T_b measured at the orthogonal channels for each AMPR receiver. For a wind-roughened ocean scene observed by AMPR, T_v and T_h are not completely uncorrelated and there exists a very weak wind-direction-dependent T_3 signal for low-to-moderate wind speeds. The error resulting from this is ignored in this study. Equations (2) and (3) are specific to the AMPR system, as measurements of T_3 and T_4 are not recorded; thus, $\overline{\overline{V(\phi')}} \cdot \overline{\mathbf{T}}$

in Eq. (1) is different than $\overline{\overline{u(\phi')}} \cdot \overline{\mathbf{T}}$ in Eq. (2). It should be noted that Eq. (2) reaches singularity at $\phi' = 0°$, which coincides with an AMPR scan angle of $\phi = 45°$ (i.e., the edge of the swath). At this angle, Eq. (3)'s solution diverges. As a result, uncertainty in input T_b increases for scan angles nearer the edge of the scan, which must be taken into consideration when interpreting results around the swath edges.

Raw AMPR measurements of radiometer counts for each frequency and polarization channel are converted to physically meaningful T_b using a two-point linear calibration in which one radiometrically "hot" and one "cold" target with known T_b values are sequentially viewed to determine radiometer system gain and T_b offset. In the typical scan sequence during OLYMPEX/RADEX, AMPR's mirror rotated to view each calibration target (hereafter simply "target") after every fourth scan. The "hot" target is controlled by a heater and is typically 318 K. However, the "cold" target is cooled using ambient air from around the aircraft, and thus its temperature varies with aircraft altitude. It should be noted that the quantity derived after applying gain and offset corrections to the radiometer counts is proportional to the total power entering the antenna aperture from all possible directions, which is known as antenna temperature. For geophysical retrievals, we are interested in total power received by the antenna main beam, which is T_b.

There are three dominant error sources in deriving T_b from antenna counts: error in estimation of receiver gain and offset, antenna pattern correction, and complicated polarization mixing geometry. For receiver gain and offset correction, the accuracy of two-point calibration depends on knowledge of hot and cold target T_b observed by AMPR. The targets are designed to be highly emissive (i.e., >99%), and their physical temperatures are measured using a platinum resistance thermometer, which yields accurate estimation of target T_b. However, in some cases, particularly for the 10.7-GHz channel, the antenna beam overilluminates the targets, yielding uncertainty in target T_b. To compensate, a correction is applied to the target temperatures, but some residual effects remain. For antenna pattern correction, accurate knowledge of AMPR's antenna pattern is needed for each scan position to model energy entering the antenna from solid angles outside of the main beam. Complicated polarization mixing geometry due to AMPR's fixed feedhorns and rotating reflector (Fig. 1) involves three key angles:

- Polarization-rotation angle (ψ), the angle between the feedhorn polarization axis and the instrument zenith direction, which is designed to be 45° for AMPR
- Reflector-normal angle (θ), the angle between the reflector normal and the reflector rotation axis; this angle typically points along the flight direction and is designed to be 45° so the antenna beam points toward nadir in the middle of an AMPR scan
- Scan angle (ϕ), the rotation angle of the mirror, with $\phi = 0°$ at nadir

Any deviation in these angles from nominal values may result in error during dual-polarization deconvolution when nominal values are assumed. In addition to these three error sources, cross-polarization leakage at the feedhorn may exist due to nonideal nature of the transducer that separates the orthogonal polarizations. A generalized model for AMPR T_b at any ϕ is given by

$$\begin{aligned} T_{b(\phi)} = {} & (1-\eta)[T_{b,v}A(\theta,\psi,\phi) + T_{b,h}B(\theta,\psi,\phi)] \\ & + \eta[T_{b,v}B(\theta,\psi,\phi) + T_{b,h}A(\theta,\psi,\phi)], \end{aligned} \tag{4}$$

where η is cross-polarization fraction, and A and B are mixing weights of the polarization (Weng et al. 2003). With nominal values of θ and ψ, values of A and B are trigonometric functions of ϕ only, which simplifies dual-polarization deconvolution.

c. *Geophysical retrievals using microwave radiometer*

Many studies have focused on obtaining geophysical information from radiometric data. Several of these efforts aimed to calculate surface rain rates (e.g., Kummerow et al. 1996; Wentz and Spencer 1998; Shin and Kummerow 2003; Bowman et al. 2009) and hydrometeor properties (e.g., Smith et al. 1994; Evans et al. 1995; Leppert and Cecil 2015) from airborne and spaceborne platforms. Additional studies utilized microwave radiometers to estimate other geophysical parameters. For example, Hong and Shin (2013) investigated methods to retrieve sea surface wind speed from spaceborne microwave radiometers. Amarin et al. (2012) and Cecil and Biswas (2017) developed methods to retrieve wind speeds around tropical systems using aircraft-based C-band microwave radiometer, while Wentz and Spencer (1998) developed an algorithm to simultaneously retrieve cloud liquid water, water vapor, wind speed, and rain rate using the Special Sensor Microwave Imager, following Wentz (1997). Similar work was performed by Biswas et al. (2017), who followed the methods of Wentz and Meissner (2000, 2007) to develop geophysical retrieval equations before applying them to AMPR data from OLYMPEX/RADEX.

The physical bases for these retrievals are rooted in properties of a calm ocean surface and atmospheric constituents when viewed at microwave frequencies. As described in Wilheit and Chang (1980), a calm ocean surface has very low emissivity due to water's large dielectric constant. Wind roughens the ocean surface and generates foam, increasing ocean surface emissivity, especially when viewed at off-nadir scan angles (Wilheit and Chang 1980). In contrast to the radiometrically cool ocean, liquid hydrometeors in the atmosphere yield higher T_b due to their higher emissivity, which is highly dependent on wavelength as Mie (1908) resonance and atmospheric absorption become more prominent at higher frequencies (Wilheit and Chang 1980). In addition, when viewed from airborne or spaceborne radiometers, atmospheric effects must be considered when computing T_b, as various atmospheric constituents (e.g., oxygen, water vapor) absorb and scatter shortwave and longwave radiation.

Utilizing these radiative properties, it is possible to retrieve column-integrated cloud liquid water, water vapor, and 10-m wind speed over the ocean using T_b at multiple frequencies within the microwave spectrum. For AMPR's channels, 10.7 GHz is most capable of viewing the ocean surface due to its relatively low attenuation, while 19.35 GHz is partially

influenced by cloud water, 37.1 GHz is strongly affected by cloud water, and 85.5 GHz is most sensitive to cloud particles (Spencer et al. 1994). In addition, high water vapor emissions may yield relatively high T_b at 85.5 GHz (Spencer et al. 1994). Section 2 below will describe how these properties were used to develop, train, and check geophysical retrieval equations for AMPR data via numerical simulations, with an uncertainty analysis from these simulations presented in section 3. Application of the retrieval equations to OLYMPEX/RADEX data will be discussed in section 4, the results of which are shown in section 5. Section 6 presents a summary and future work.

2. Forming the retrieval equations

The methods discussed herein and in section 4 follow Biswas et al. (2017). To develop multiple-linear regression equations for the geophysical retrievals, 523 176 globally distributed atmospheric profiles from the Global Data Assimilation System (GDAS; NCEP 2000) were used to form a T_b dataset. Cloud-top and cloud-bottom properties were obtained from ocean climatology (Wisler and Hollinger 1977). When deriving this physical T_b dataset, instead of using the sea surface temperature (SST) and wind speed data from the GDAS profiles, SST was randomly varied from 0° to 30°C and wind speed was randomly varied from 0 to 20 m s^{-1}, ignoring wind direction. This was done to decouple the atmosphere and sea surface when forming the T_b dataset that would be used to train the retrieval equations.

The resulting physical T_b dataset was used in a radiative transfer model (RTM) to simulate T_b that would be observed by AMPR. Within the RTM, following Biswas et al. (2013), atmospheric absorption coefficients were calculated using Rosenkranz models for cloud liquid water (Liebe et al. 1991), oxygen (Liebe et al. 1991), nitrogen (Rosenkranz 1993), and water vapor (Rosenkranz 1998). While residual uncertainties in these models must be considered, it is worth noting that these absorption models were used in several independent studies during the Global Precipitation Measurement (GPM) cross-calibration activity (Biswas et al. 2013), and have been found to provide an acceptable standard over the AMPR frequency range. The emissivity model in Meissner and Wentz (2012) was used to compute surface emission and scattering; this model was developed and tested with many well-calibrated microwave radiometers (Meissner and Wentz 2012), and is acceptable for use with AMPR's frequencies.

These models yielded the following general expression, which is adapted from Meissner and Wentz (2012), for top-of-atmosphere T_b:

$$T_{B,p} = T_{\mathrm{BU}} + \tau E_p T_s + \tau T_{B\Omega}, \tag{5}$$

where $T_{B,p}$ is top-of-atmosphere T_b, T_{BU} is upwelling atmospheric T_b, τ is atmospheric transmissivity, $E_p = 1 - R_p$ where R_p is sea surface reflectivity, T_s is SST, and $T_{B\Omega}$ is downwelling sky radiation scattered by the ocean surface. AMPR-observed T_b values were simulated for Earth-incidence angle (EIA) values of 0° to 50° at a 0.2° increment, and 0.5 K of Gaussian noise was introduced into the RTM to maintain stability (Wentz and Meissner 2000). This 0.5 K of Gaussian noise is within AMPR's noise-equivalent differential temperature (NEDT), which we determined to be 0.5–1.0 K during OLYMPEX/RADEX (not shown), and thus represents the uncertainty in AMPR-observed T_b values. Since this noise was introduced into the simulated T_b values before their use in training the regression equations, the noise is uncorrelated between the two polarizations. Other sources of uncertainty exist in the simulations, such as uncertainty in GDAS SST, but these effects have been neglected due to their relatively small magnitude. For example, Bhargava et al. (2018) noted that GDAS SST was robust enough to be used as "truth" values in their study, and yielded an average bias ≤ 0.5 K (albeit, during the month of June). We have also neglected uncertainties in EIA, as these are typically around 0.1°, which results in T_b uncertainty of 0.1–0.2 K (albeit, for conically scanning microwave radiometers; Berg et al. 2013).

Multiple linear regression was performed on the simulated T_b data [from Eq. (5)] to derive coefficients for the geophysical retrieval equations, following Wentz and Meissner (2000). The geophysical parameters for which equations were developed in this study were: column-integrated cloud liquid water (CLW), column-integrated total precipitable water [herein "water vapor" (WV)], and 10-m wind speed over the ocean (WS). The general forms of the retrieval equations are

$$\begin{aligned}\mathrm{CLW(mm)} = {} & a_0 + a_1 \ln(290 - T_{b19v}) + a_2 \ln(290 - T_{b19h}) + a_3 \ln(295 - T_{b85v}) \\ & + a_4 \ln(295 - T_{b85h}),\end{aligned} \tag{6}$$

$$\begin{aligned}\mathrm{WV(mm)} = {} & a_0 + a_1 T_{b10v} + a_2 T_{b10h} + a_3 \ln(290 - T_{b19v}) + a_4 \ln(290 - T_{b19h}) \\ & + a_5 \ln(290 - T_{b37v}) + a_6 \ln(290 - T_{b37h}) + a_7 \mathrm{SST},\end{aligned} \tag{7}$$

$$\begin{aligned}\mathrm{WS(m\ s^{-1})} = {} & a_0 + a_1 \ln(285 - T_{b10v}) + a_2 \ln(285 - T_{b10h}) + a_3 T_{b10v}^2 + a_4 T_{b10h}^2 \\ & + a_5 (T_{b10v} T_{b10h}) + a_6 T_{b19v} + a_7 T_{b19h} + a_8 T_{b19v}^2 + a_9 T_{b19h}^2 + a_{10} (T_{b19v} T_{b19h}) \\ & + a_{11} T_{b37v} + a_{12} T_{b37h} + a_{13} T_{b37v}^2 + a_{14} T_{b37h}^2 + a_{15} (T_{b37v} T_{b37h}) + a_{16} \mathrm{SST},\end{aligned} \tag{8}$$

where the "a" terms are regression coefficients; T_b is in kelvins; v and h subscripts indicate vertical and horizontal polarization, respectively; the 10, 19, 37, and 85 subscripts indicate the 10.7-, 19.35-, 37.1-, and 85.5-GHz AMPR channels, respectively; and

SST is sea surface temperature in kelvins. Coefficients in Eqs. (6)–(8) were generated for each AMPR EIA as seen in Fig. 2. The AMPR channels used in Eqs. (6)–(8) and the modifications to each T_b (e.g., use of natural logarithms) were determined via an empirical analysis (not shown) during which more than 100 regression equations were tested and the combinations of channels that yielded the most optimal tradeoffs between low retrieval error (i.e., how error in the retrieved variable is affected by variations in that variable) and crosstalk errors (i.e., how error in the retrieved variable is affected by variations in other variables) were selected. As an initial test of Eqs. (6)–(8), mean retrieval and crosstalk errors (i.e., deviations herein) across the 523 176 GDAS simulations were calculated using the differences between the geophysical values output from Eqs. (6)–(8) and the same geophysical parameters observed in the GDAS profiles, averaged across all EIAs. In addition to mean retrieval and crosstalk error, the retrieval root-mean-square deviation (RMSD) was calculated to obtain a more robust measurement of retrieval uncertainty. For eventual comparison with dropsonde data from OLYMPEX/RADEX, which, as will be discussed in sections 4 and 5, had far fewer data points available than the simulations, median absolute deviation (MedAD) was also calculated for all AMPR pixels (i.e., 0 to n) as

$$\text{MedAD} = \text{median}(|\text{predicted}_{0,n} - \text{observed}_{0,n}|). \quad (9)$$

It should be noted that Eq. (8) is designed to calculate any 10-m wind speed value over the ocean, which differs from past methods (e.g., Wilheit and Chang 1980; Hong and Shin 2013) that utilized different equations for different ranges of wind speeds. This reduces artifacts that may occur when comparing multistep calculations to those obtained via other methods, but may increase retrieval error for lower wind speeds (e.g., Hong and Shin 2013). Furthermore, Eq. (7) does not utilize AMPR's 85.5-GHz channel, despite the potential influence from high WV at this frequency (e.g., Spencer et al. 1994). This decision was made based on a brief sensitivity test, which showed little improvement in WV retrieval RMSD compared to Eq. (7) (i.e., difference of approximately 3.0×10^{-2} mm) when 85.5-GHz data were included in the regression equation, but this may be explored further in future work.

Last, it has been demonstrated how WV is strongly correlated with SST (e.g., Stephens 1990). Our decision to include SST in Eq. (7) as a regression variable resulted from testing various methods to remove WV cross-track stripes observed in Biswas et al. (2017), which were largely successful. However, variance in our WV retrievals during a given flight are not related to SST, since, as we discuss in section 4, we used the median SST observed during the flight as the SST value for *all* AMPR pixels during that flight. To confirm this, a principal component analysis (PCA; not shown) was performed, which, after standardizing the data, demonstrated that approximately 97.8% of the variance in simulated T_b was explained by the first two principal components. The correlation between SST and these two principal components was extremely small (i.e., magnitude of 10^{-10} or less), further indicating essentially no variance explanation from the SST term. Thus, variations in WV calculated via Eq. (7) were solely due to variations in AMPR T_b during the flight.

In this same regard, Wilheit and Chang (1980) noted that including T_b from a frequency around 37.1 GHz only slightly improved WS retrieval. During our sensitivity tests, we also noted minimal improvement in WS retrieval after including 37.1-GHz T_b. However, we also noted that 37.1-GHz T_b significantly reduced cross-track stripe artifacts that resulted from use of a single WS equation across all ranges of wind speed, which warranted its inclusion in Eq. (8).

3. Statistical results of retrieval simulations

This section presents the results of geophysical parameters calculated using Eqs. (6)–(8), with simulated T_b values from Eq. (5) as inputs, compared to geophysical values obtained from the 523 176 GDAS profiles. Retrieval RMSD for each parameter as a function of EIA is shown in Fig. 3. Starting with CLW, the trend of CLW versus EIA in Fig. 3 demonstrates that retrieval error depends strongly on EIA. For EIA around 0°, CLW RMSD was at its maximum, 0.116 mm, primarily due to the similarity between horizontally and vertically polarized T_b at nadir (e.g., Wilheit and Chang 1980), which makes it difficult to interpret differences between T_b from AMPR's orthogonal receivers for near-nadir EIAs. CLW RMSD decreased farther from nadir as horizontally and vertically polarized T_b values diverge (all else being equal), reaching a minimum of 9.8×10^{-2} mm around 43°. The slight RMSD increase after EIA = 43° was likely due to the greater distance in the atmosphere through which the AMPR signal must travel.

CLW retrieval and crosstalk errors averaged across all EIAs for a range of geophysical values can be found in Fig. 4. From Fig. 4, mean CLW retrieval error was around 0 mm for the 0.025–0.3 mm CLW range and standard deviation remained within 0.1 mm, indicating that Eq. (6) produced fairly consistent results across a range of CLW. Crosstalk errors of CLW with WV, WS, and SST were also fairly low, albeit less stable than retrieval error across the range of values considered. Mean CLW–WS crosstalk error increased for WS greater than 15 m s^{-1} but remained less than roughly 0.05 mm, and standard deviation was around 0.1 mm. CLW–WV crosstalk error was more chaotic, with mean error nearly unbiased for WV around 0 mm but increasing in magnitude to approximately 0.1 mm for WV around 60 mm, and standard deviation increased from about 0.05 mm for WV near 0 mm to more than 0.15 mm for WV greater than 30 mm. This may have been due to increased attenuation from higher WV concentration resulting in higher CLW–WV crosstalk error (e.g., Liebe 1985, 1989). Mean CLW–SST crosstalk error gradually increased from about −0.02 to 0.04 mm across the 0°–30°C range of SST considered, and standard deviation remained about 0.1–0.15 mm. Deviations in CLW retrieval and crosstalk values may have also occurred due to inaccuracies in the assumptions present in Eq. (6) when attempting to model CLW based on T_b values, as well as residual uncertainties from the radiative models discussed in section 2. The average CLW retrieval RMSD was 0.11 mm and median retrieval MedAD was 2.26×10^{-2} mm.

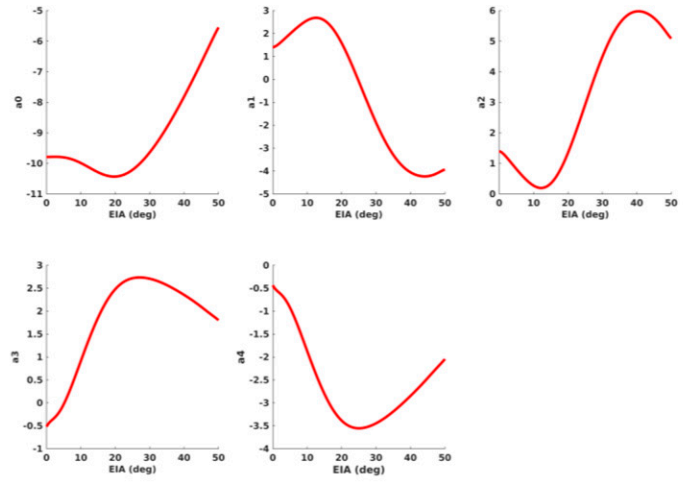

$$\mathrm{CLW\ (mm)} = a_0 + a_1 \cdot \ln(290 - T_{b19v}) + a_2 \cdot \ln(290 - T_{b19h}) + a_3 \cdot \ln(295 - T_{b85v}) + a_4 \cdot \ln(295 - T_{b85h})$$

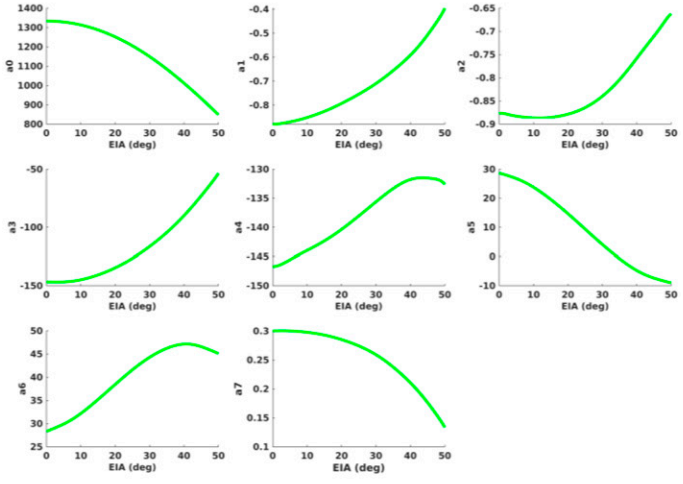

$$\mathrm{WV\ (mm)} = a_0 + a_1 \cdot T_{b10v} + a_2 \cdot T_{b10h} + a_3 \cdot \ln(290 - T_{b19v}) + a_4 \cdot \ln(290 - T_{b19h}) + a_5 \cdot \ln(290 - T_{b37v}) + a_6 \cdot \ln(290 - T_{b37h}) + a_7 \cdot \mathrm{SST}$$

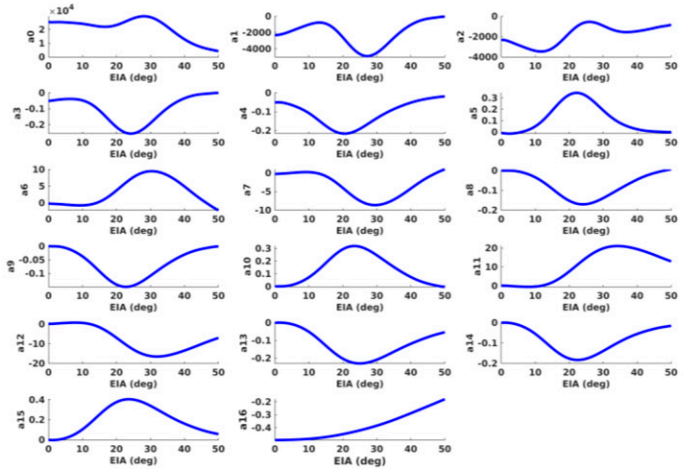

$$\mathrm{WS\ (m\ s^{-1})} = a_0 + a_1 \cdot \ln(285 - T_{b10v}) + a_2 \cdot \ln(285 - T_{b10h}) + a_3 \cdot T_{b10v}^{\ 2} + a_4 \cdot T_{b10h}^{\ 2} + a_5 \cdot (T_{b10v} \cdot T_{b10h}) + a_6 \cdot T_{b19v} + a_7 \cdot T_{b19h} + a_8 \cdot T_{b19v}^{\ 2} + a_9 \cdot T_{b19h}^{\ 2} + a_{10} \cdot (T_{b19v} \cdot T_{b19h}) + a_{11} \cdot T_{b37v} + a_{12} \cdot T_{b37h} + a_{13} \cdot T_{b37v}^{\ 2} + a_{14} \cdot T_{b37h}^{\ 2} + a_{15} \cdot (T_{b37v} \cdot T_{b37h}) + a_{16} \cdot \mathrm{SST}$$

FIG. 2. Plots of the regression coefficients in the retrieval equations for (top left) cloud liquid water (red lines), (middle left) water vapor (green lines), and (bottom left) 10-m wind speed over the ocean (blue lines) as a function of AMPR Earth-incidence angle (EIA). (right) Equations (6)–(8) are shown next to their respective variable.

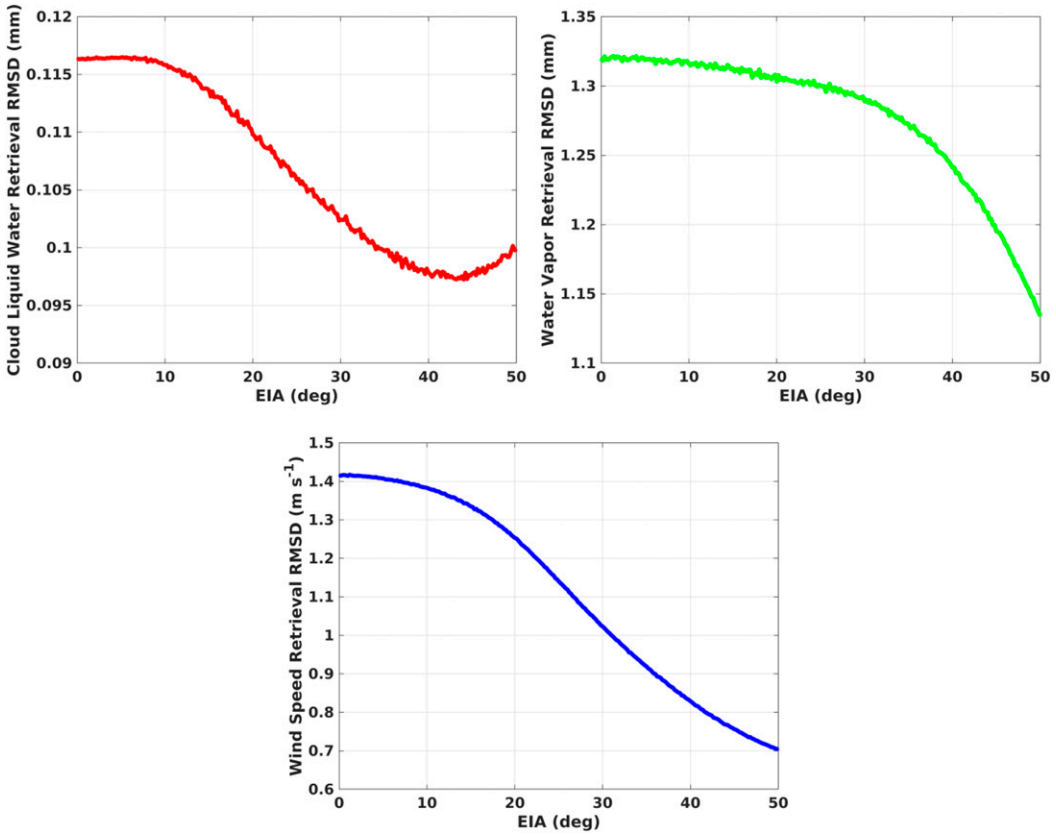

FIG. 3. Plots of RMSD as a function of EIA for the simulated retrievals of (top left) CLW (red line), (top right) WV (green line), and (bottom) WS (blue line). The RMSD values at each EIA were averaged across all GDAS simulations. In the RMSD calculations, the "predicted" CLW, WV, and WS values were those from Eqs. (6)–(8), and the "observed" values were the geophysical parameters from the GDAS profiles.

Next, WV retrieval and crosstalk errors are shown in Fig. 5, while WV retrieval RMSD as a function of EIA can be found in Fig. 3. As with CLW, WV RMSD reached a maximum of 1.32 mm around nadir, but decreased exponentially with increasing EIA, likely owing to increasing differences in horizontally and vertically polarized T_b. In general, WV error trends in Fig. 5 were less chaotic than those for CLW in Fig. 4, which may have been due to higher CLW values being less common in the GDAS data, leading to chaotic error trends as a result of lower sample size. Mean WV retrieval error was around 0 mm for WV values less than 30 mm, with a standard deviation of approximately 1 mm. Mean error was slightly negative between 30 and 50 mm, reaching peak magnitude of 0.5 mm around 40 mm, with a standard deviation around 1.5 mm. Once WV increased above 50 mm, retrieval error increased considerably, with mean error of 1 mm and standard deviation around 1.5 mm for WV of 60 mm and greater. This trend of WV error magnitude increasing with increasing WV is similar to CLW–WV crosstalk error increasing with increasing WV in Fig. 4, possibly due to increased attenuation. Further examining Fig. 5, WV crosstalk errors with CLW, WS, and SST were all fairly stable, with near-zero mean WV crosstalk error and standard deviation of 1–1.5 mm across the range of values considered. Average WV retrieval RMSD was 1.28 mm and median retrieval MedAD was 0.22 mm, indicating that Eq. (7) provided fairly precise WV estimation.

Last, WS retrieval and crosstalk errors are presented in Fig. 6, while WS RMSD as a function of EIA can be found in Fig. 3. From Fig. 3, similar to CLW and WV, the WS RMSD reached a maximum around 1.41 m s^{-1} at nadir before decreasing with increasing EIA. It can be noted that the range of WS RMSD in Fig. 3 is the largest of the three parameters, owing largely to its dependence on differences between horizontally and vertically polarized T_b (e.g., Wilheit and Chang 1980). In Fig. 6, as with WV, WS crosstalk errors with WV, CLW, and SST were fairly uniform, with a mean around 0 m s^{-1} and standard deviation of approximately 1 m s^{-1} across the range of WV, CLW, and SST examined; the main exception is WS-SST crosstalk error for SST around 0°–3°C, where mean error varied from about −0.8 to −0.4 m s^{-1}. Thus, as with Eq. (7) for WV, Eq. (8) provided a fairly precise estimate of 10-m WS across a variety of WV, CLW, and SST. Mean WS retrieval error fluctuated from negative values for WS less than 5 m s^{-1}, to positive values for WS between 5 and 15 m s^{-1}, and slightly negative for WS greater than 15 m s^{-1}. Underestimation of WS less than 5 m s^{-1} makes sense physically, since the 10.7-GHz AMPR channel is sensitive to SST and surface disturbances (e.g., Wentz and Meissner 2007;

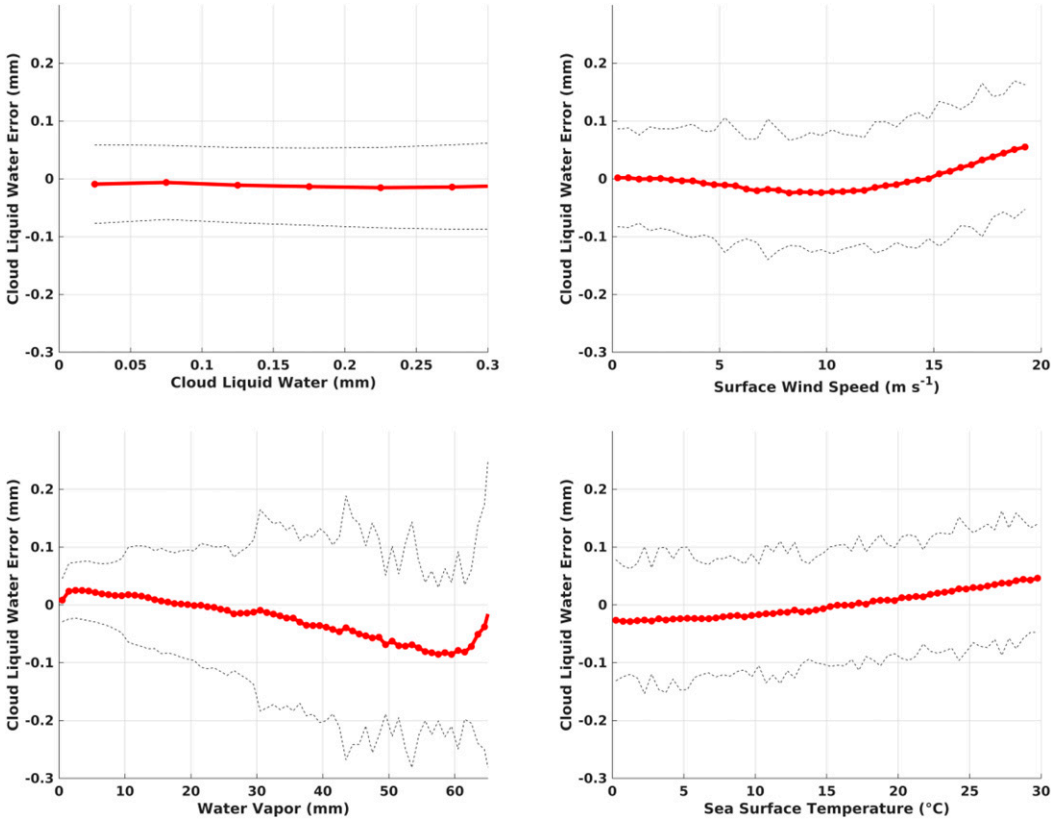

FIG. 4. Plots of (top left) cloud liquid water retrieval error and (top right) the cloud liquid water crosstalk errors with 10-m wind speed, (bottom left) water vapor, and (bottom right) sea surface temperature calculated using Eqs. (6)–(8), with simulated AMPR T_b as input values, compared to geophysical values obtained from the NCEP GDAS atmospheric profiles. The red dotted line in each plot indicates the mean error averaged across all EIAs, and the dashed lines in each plot indicate one standard deviation in the error across all EIAs.

Hong and Shin 2013), but wind speeds less than 5 m s^{-1} may not disturb the ocean surface considerably from a flat calm, yielding little response in 10.7-GHz T_b and, thus, wind speed underestimation (e.g., Wilheit and Chang 1980; Hong and Shin 2013). Conversely, the slight overestimation in WS between 5 and 15 m s^{-1} may be due to greater surface disturbance leading to greater response in the 10.7-GHz channel than expected. Other sources of error exist, such as use of multiple-linear regression for the nonlinear relation between WS and T_b (Wilheit and Chang 1980), residual uncertainty from the radiative models in section 2, and other inaccuracies in the assumed structure of Eq. (8) for deriving WS from T_b. However, WS retrieval errors were relatively low under most conditions in Fig. 6, with mean error magnitude and standard deviation less than 1 m s^{-1} for WS between 3 and 19 m s^{-1}. The average WS retrieval RMSD was 1.11 m s^{-1}, and median retrieval MedAD was 0.55 m s^{-1}.

4. Methods for testing the retrieval equations

This section details how Eqs. (6)–(8) were applied to data collected during OLYMPEX/RADEX. In this study, we evaluate the performances of these equations over four ER-2 flights: 23 November, 24 November, 10 December, and 13 December 2015. As part of our analysis, we first performed a T_b calibration for all AMPR data collected during these flights to remove biases resulting from the four quantities in Eq. (4). After deconvolving the raw AMPR T_b data into pure horizontally and vertically polarized T_b, following Yang et al. (2013), any departure in observed T_b from a predicted value during each flight constituted a T_b bias via the relation

$$T_{b,\text{bias}} = T_{b,\text{observed}} - T_{b,\text{simulated}}. \tag{10}$$

In our analysis, the $T_{b,\text{observed}}$ values were those obtained during the ER-2 flights, while the $T_{b,\text{simulated}}$ values were calculated from GDAS data points throughout each AMPR flight path using Eq. (5). However, unlike the calculations discussed in section 2, we utilized the SST and wind speed values from the GDAS profiles throughout each flight to provide an accurate representation of the atmospheric conditions during the flights (i.e., SST and wind speed were not randomly selected when calibrating the AMPR T_b data).

The T_b at each scan angle was averaged for each case to evaluate mean bias in horizontally and vertically polarized deconvolved T_b, seen in Fig. 7. In general, observed horizontally

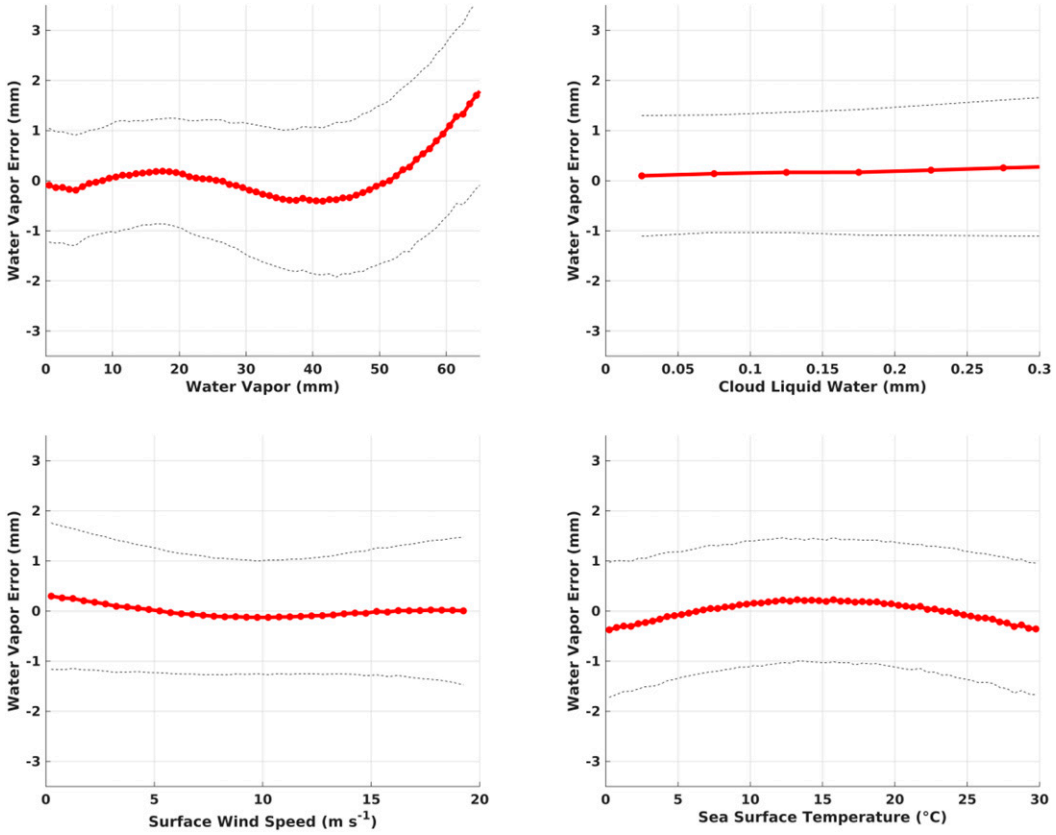

FIG. 5. As in Fig. 4, but for (top left) water vapor retrieval error and (top right) the water vapor crosstalk errors with cloud liquid water, (bottom left) 10-m wind speed, and (bottom right) sea surface temperature.

polarized AMPR T_b tends to be more positively biased while vertically polarized T_b tends to be more negatively biased. To account for this, the T_b bias resulting from all four parameters in Eq. (4) was calculated for each scan angle during each flight (not shown), and the resulting values were subtracted from the T_b biases in Fig. 7, yielding the values in Fig. 8. This T_b bias correction was applied to all AMPR scans during the four case dates prior to their use in the geophysical retrievals. In each OLYMPEX/RADEX case, AMPR surface pixels were masked from the retrieval analyses if they were over land, based on visual inspection of the data, or if the ER-2 roll angle was greater than 1°.

The performances of Eqs. (6)–(8) were analyzed via two methods: comparisons with an independent retrieval method and comparisons with in situ observations. In this study, the selected independent retrieval method was a one-dimensional variational (1DVAR) technique (Duncan and Kummerow 2016). While the 1DVAR presented in Duncan and Kummerow (2016) was developed for use with conically scanning microwave radiometers, such as the GPM Microwave Imager (GMI), Schulte and Kummerow (2019) and Schulte et al. (2020) demonstrated how 1DVAR is also applicable to cross-track-scanning radiometers. The 1DVAR is an optimal estimation technique, based on Bayes's theorem, used to determine the state of the atmosphere based on input T_b values and an input a priori vector of state variables, which is needed to constrain the solution (Duncan and Kummerow 2016; Schulte and Kummerow 2019; Schulte et al. 2020). This inverse method of estimating the atmosphere's state from input T_b, as shown and discussed in Schulte and Kummerow (2019) and Schulte et al. (2020) based on the full mathematical description provided in Rodgers (2000), may be expressed mathematically as

$$\mathbf{y} = f(\mathbf{x}, \mathbf{b}) + \varepsilon, \tag{11}$$

where $\mathbf{y}$ is a vector containing the observed T_b values, $\mathbf{x}$ is a vector containing the atmospheric parameters of interest, $\mathbf{b}$ is a vector containing additional atmospheric features that influence T_b but are not directly of interest, f is a forward model that relates the atmospheric variables to the observed T_b values, and ε represents errors caused by noise, uncertainties in the atmospheric parameters contained within vector $\mathbf{b}$, etc.

The one-dimensional variational technique provides a method by which the vector $\mathbf{x}$ in Eq. (11) can be determined via inversion using the observed T_b values, a priori information about the state of the atmosphere, and an estimation of errors. Using these inputs, 1DVAR calculates a cost function that considers the difference between a given solution [from Eq. (11)] and the a priori state, as well as the difference

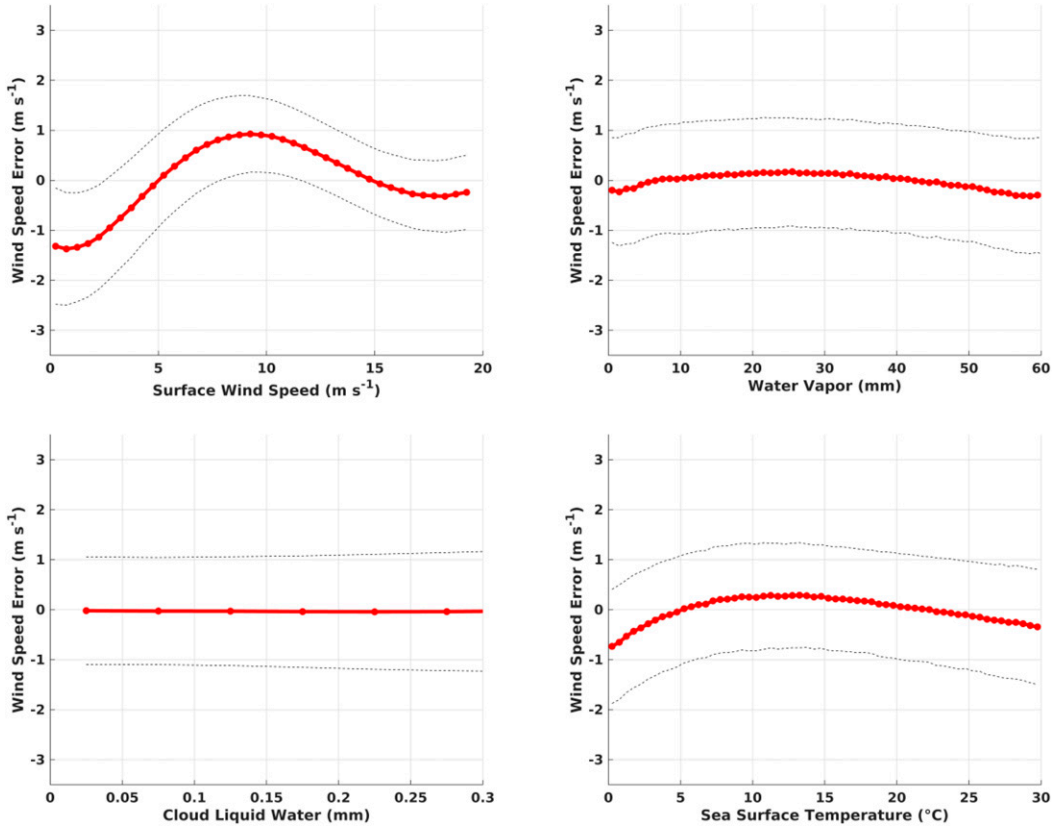

FIG. 6. As in Fig. 4, but for (top left) 10-m wind speed retrieval error and (top right) the 10-m wind speed crosstalk errors with water vapor, (bottom left) cloud liquid water, and (bottom right) sea surface temperature.

between the observed T_b values and the T_b values predicted by the forward model in Eq. (11):

$$\Phi = (\mathbf{x} - \mathbf{x}_a)^{\mathrm{T}}\mathbf{S}_a^{-1}(\mathbf{x} - \mathbf{x}_a) + [\mathbf{y} - f(\mathbf{x},\mathbf{b})]^{\mathrm{T}}\mathbf{S}_y^{-1}[\mathbf{y} - f(\mathbf{x},\mathbf{b})], \tag{12}$$

where $\mathbf{x}_a$ is the vector containing the a priori information, $\mathbf{S}_a$ is the error covariance matrix for the a priori, and $\mathbf{S}_y$ is the error covariance matrix for uncertainties in the forward model and the T_b observations (Duncan and Kummerow 2016; Schulte and Kummerow 2019; Schulte et al. 2020). Using Newton's method and assuming the error distribution is Gaussian, Eq. (12) is solved iteratively until the gradient in Φ with respect to x reaches a minimum, at which point 1DVAR has converged on a solution (i.e., CLW, WV, and WS herein) based on the input T_b values (Duncan and Kummerow 2016).

In this study, the values of y in Eq. (11) were the observed T_b values at the four AMPR frequencies collected during the selected OLYMPEX/RADEX flights, and the vector $\mathbf{x}$ included CLW, WV, and SST. The a priori state of the atmosphere was provided using Goddard Earth Observing System Model, version 5 (GEOS-5), data from around the time and location of the selected ER-2 flight path. With these inputs, 1DVAR was used to compute CLW, WV, and WS for the same cases and AMPR pixels as Eqs. (6)–(8). In Eqs. (7) and (8), the median SST, calculated from the GDAS data points along the ER-2 flight path for the selected case, was used; median SST was chosen based on an empirical analysis (not shown) that indicated slightly improved agreement between 1DVAR and Eqs. (7) and (8) compared to using mean SST. For qualitative comparisons between the two methods, retrieved values throughout each ER-2 flight were visualized using 2D histograms for all nonmasked pixels. For quantitative comparisons, MedAD between the two retrieval methods was calculated for all pixels via Eq. (9), as was RMSD, where the values from Eqs. (6)–(8) were used as "predicted" for the given geophysical parameter and 1DVAR's retrieval for the same pixel and geophysical parameter was "observed."

Similar to Cecil and Biswas (2017), WS calculated using Eq. (8) was also compared with 10-m winds calculated using dropsonde data from the Advanced Vertical Atmospheric Profiling System (AVAPS; Hock and Young 2017), which was flown on the NASA DC-8 aircraft during OLYMPEX/RADEX (Houze et al. 2017). WV calculated using Eq. (7) was also compared with total precipitable water (TPW) calculated from AVAPS. CLW comparisons were not made due to the potential for very high spatial and temporal CLW variability, but could be performed in future work. Following Uhlhorn et al. (2007), if AVAPS data were available below 500 m AGL but unavailable below 150 m AGL, 10-m wind speed was calculated via

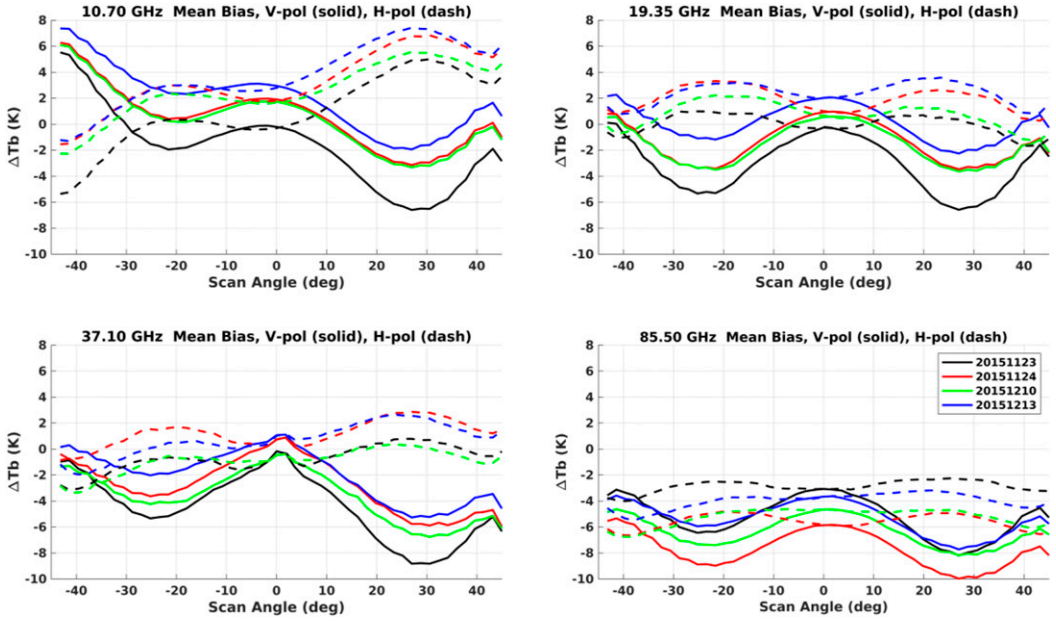

FIG. 7. Plots of the mean bias in observed AMPR T_b from four ER-2 flights: 23 Nov (black lines), 24 Nov (red lines), 10 Dec (green lines), and 13 Dec 2015 (blue lines) compared to the simulated AMPR T_b values from the GDAS profiles throughout each flight. The four panels illustrate the mean T_b bias at (top left) 10.7-, (top right) 19.35-, (bottom left) 37.1-, and (bottom right) 85.5-GHz frequencies for the four case study dates. The x axes denote AMPR's scan angle, with negative (positive) values located on the left (right) half of the scan swath, and 0° corresponding to nadir. Within each plot, the solid lines represent the deconvolved vertically polarized T_b at that frequency, while the dashed lines represent the deconvolved horizontally polarized T_b values. All T_b biases were calculated using Eq. (10). Adapted from Biswas et al. (2017).

$$\mathrm{WS}_{10} = 0.8\,\overline{\mathrm{WS}_{0,500}}, \tag{13}$$

where WS_{10} is 10-m wind speed, and $\overline{\mathrm{WS}_{0,500}}$ is mean AVAPS-measured wind speed between 500 m AGL and the surface. If AVAPS data were available below 150 m AGL, 10-m wind speed was calculated using

$$\mathrm{WS}_{10} = \overline{\mathrm{WS}_{0,150}} \times [1.0314 - 4.071 \times 10^{-3}(z) + 2.465 \times 10^{-5}(z^2) - 5.445 \times 10^{-8}(z^3)], \tag{14}$$

where $\overline{\mathrm{WS}_{0,150}}$ is mean AVAPS-measured wind speed between 150 m AGL and the surface, and z is mean height AGL for wind data recorded below 150 m AGL. While these equations were derived to increase accuracy in radiometer estimations of 10-m hurricane-force winds (e.g., $>50\,\mathrm{m\,s^{-1}}$), they are applicable at lower wind speeds (Uhlhorn et al. 2007). TPW was calculated using all AVAPS levels where dewpoint and pressure data were available via

$$\mathrm{TPW} = \frac{1}{\rho g}\int_{p_1}^{p_2} r(p)\,dp \approx \frac{1}{\rho g}\left[\frac{r(p_2) + r(p_1)}{2}\right](p_2 - p_1), \tag{15}$$

where ρ is density of liquid water, g is gravitational acceleration, and $r(p)$ is mixing ratio integrated between pressure levels p_1 and p_2 (AMS 2019).

Since AVAPS and AMPR were flown on separate aircraft, there were spatial and temporal differences in their datasets. Thus, WV and WS calculated using AVAPS and AMPR data were compared at two times for each available dropsonde: at the time of AVAPS minimum height (i.e., spatial offset between AMPR and AVAPS) and when AMPR passed over the location where AVAPS reached its minimum height (i.e., temporal offset between AMPR and AVAPS). Dropsondes launched when the ER-2 was not over the ocean were not considered. When comparing AMPR and AVAPS, all AMPR scans during the time period of approximately 5 min before the time of interest (i.e., the time of AVAPS minimum height or the time AMPR passed over the AVAPS minimum height location) to 5 min after the time of interest were used to calculate an average AMPR-derived WV and WS. In cases where the ER-2 was over land or turning when AVAPS reached minimum height, AMPR scans during the time period from 15 to 5 min before AVAPS minimum height were used instead. These 10-min periods were selected to provide larger-scale averages of WV and WS around the time of interest to account for spatial and temporal offsets between the two datasets. The dates, times, and locations of all dropsondes analyzed are shown in Table 1. MedAD [Eq. (9)] was used to compare WV and WS from AVAPS and AMPR data, with AVAPS used as the "observed" quantity. MedAD was utilized in this study due to the small AVAPS sample size, as will be discussed in section 5. Since outliers will heavily influence RMSD in a small sample size, MedAD better represents the calculated AMPR–AVAPS deviations.

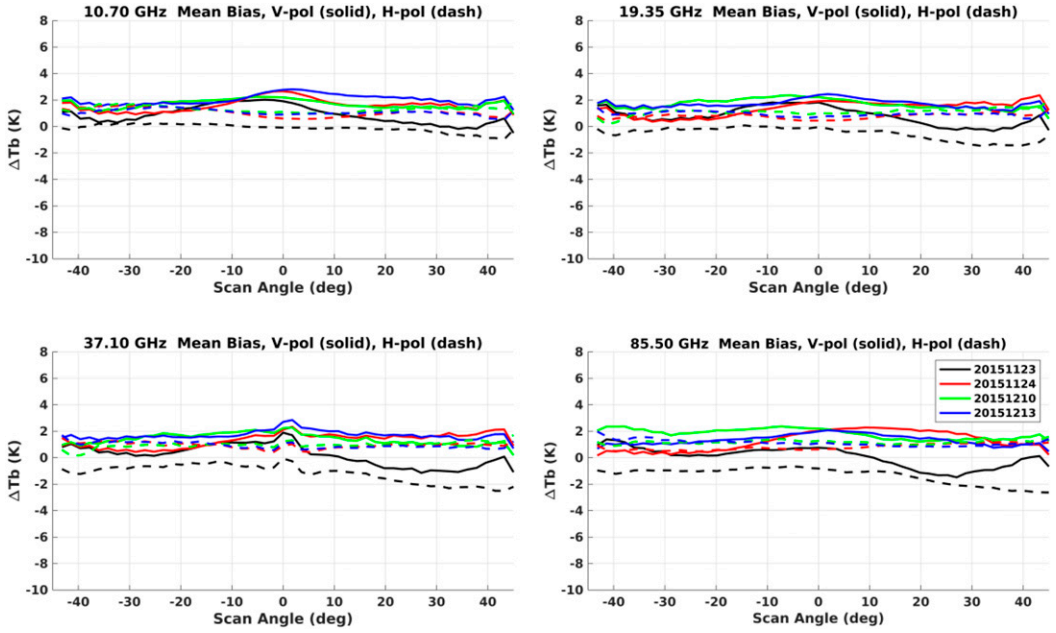

FIG. 8. As in Fig. 7, except the T_b biases caused by cross-polarization fraction (η), reflector-normal angle (θ), polarization-rotation angle (ψ), and the scan angle of the antenna (ϕ) in Eq. (4) have been removed from the calculated differences in observed and simulated T_b in Eq. (10). Adapted from Biswas et al. (2017).

5. Retrieval equations applied to OLYMPEX/RADEX cases

This section illustrates the utility of Eqs. (6)–(8) when applied to AMPR data from OLYMPEX/RADEX. Comparisons with independent methods (i.e., 1DVAR and AVAPS) are presented. For brevity, in-depth examples will be shown for two OLYMPEX/RADEX cases, but the performances of Eqs. (6)–(8) compared to 1DVAR and AVAPS will be summarized for all four dates examined.

a. *Case 1: 24 November 2015*

The 24 November 2015 case featured a relatively high-amplitude positively tilted trough axis over the study region, with 1000-hPa geopotential heights as low as 30 m within the low pressure center that propagated through the study region less than 6 h before the ER-2 flight [University of Wyoming (UWYO); UWYO 2019]. Deconvolved horizontally polarized AMPR T_b from a portion of the flight can be found in Fig. 9, during which some weak precipitation can be observed (e.g., around 2020–2033 UTC), allowing for equation testing in clear air and weak precipitation. To further support the inference of precipitation, data from the ground-based NASA S-band dual-polarimetric (NPOL) radar (Wolff et al. 2017) were examined. Two NPOL range–height indicator (RHI) scans through the region of precipitation sampled by AMPR around 2020–2033 UTC are presented in Fig. 10, which were created using the Python ARM Radar Toolkit (Helmus and Collis 2016).

TABLE 1. The date of each AVAPS dropsonde analyzed in this study, the time the dropsonde reached its minimum (min) recorded height, the latitude and longitude (lat, lon) location of the dropsonde at its minimum recorded height, the (lat, lon) location of AMPR at the time the dropsonde reached its min height, and the time AMPR passed over the AVAPS min height (lat, lon) location. An asterisk in the fourth column indicates that the listed (lat, lon) represents AMPR's location 10 min before AVAPS reached min height in cases where AMPR was over land at the actual time of AVAPS min height.

Date	Time of AVAPS min height (UTC)	AVAPS (lat, lon) at min height (°)	AMPR (lat, lon) at AVAPS min height (°)	Time AMPR reached AVAPS min height location (UTC)
23 Nov 2015	1741:13	47.2021, −126.639	47.7750, −126.151	1757:53
23 Nov 2015	1921:08	48.1935, −125.960	47.5564, −125.057	1702:43
23 Nov 2015	1936:25	47.6687, −124.999	48.0426, −125.933	1942:25
23 Nov 2015	1948:48	48.1808, −125.908	47.9237, −125.549*	1906:53
24 Nov 2015	1803:57	47.1599, −125.640	46.6466, −126.472	2036:05
24 Nov 2015	1813:57	46.8343, −126.884	47.0178, −126.447	1801:19
10 Dec 2015	1734:17	46.8752, −125.143	47.0766, −124.946*	1829:58
10 Dec 2015	1841:48	46.8564, −125.194	47.0697, −124.961*	1721:56
13 Dec 2015	1721:08	47.7733, −125.627	47.5862, −125.275*	1751:36

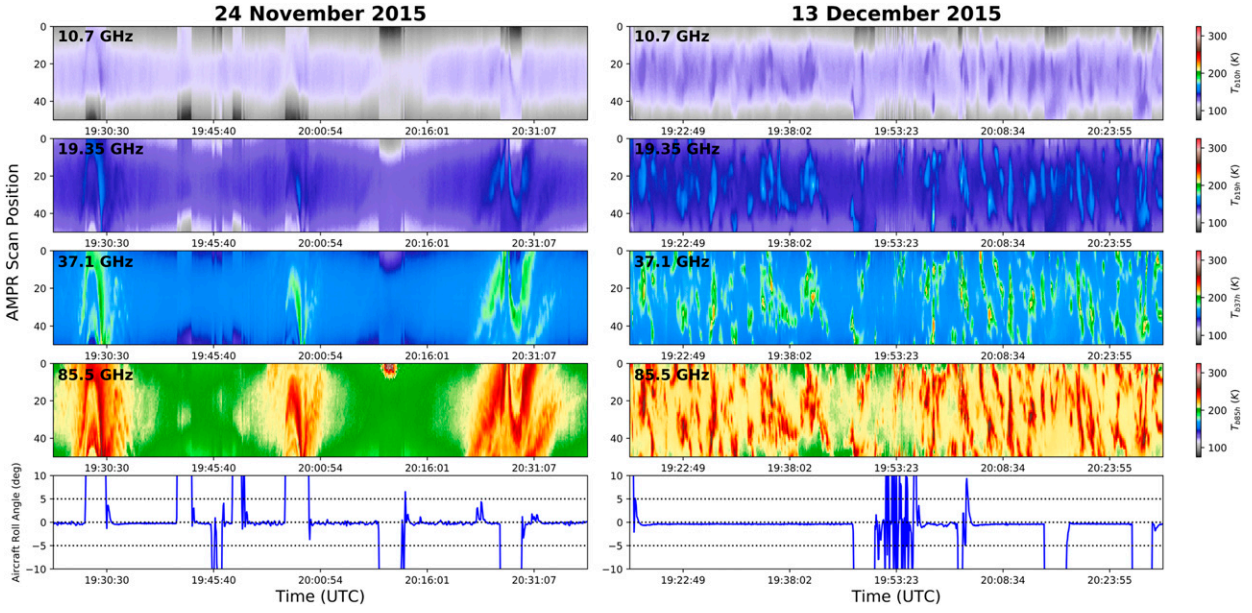

FIG. 9. Deconvolved horizontally polarized AMPR brightness temperatures at the frequencies (top) 10.7, (second from top) 19.35, (middle) 37.1, and (second from bottom) 85.5 GHz during portions of the ER-2 flights on (left) 24 Nov and (right) 13 Dec 2015. AMPR scan positions are shown on the *y* axis in the top four rows for each date, with scan position 25 corresponding to nadir. (bottom) Aircraft roll angle for each date.

Regions of equivalent radar reflectivity factor (Z_H) > 30 dB*Z* can be seen at the lowest elevation angles of both RHI scans, especially at 224° azimuth, which are indicative of moderate rainfall rates at S band (e.g., Straka et al. 2000).

Using the 24 November data in Fig. 9, CLW, WV, and WS calculated via Eqs. (6)–(8), respectively, can be found in Fig. 11. From Fig. 11, it can be seen further that weak precipitation was present among clear air, such as 2031 UTC when CLW and WV increased to roughly 0.5 and 20 mm, respectively. However, in most pixels, CLW and WV were less than 0.5 and 20 mm, respectively. WS was slightly less uniform, ranging from near 0 to 15 m s^{-1} throughout Fig. 11. For the same flight portion, 1DVAR retrievals of CLW, WV, and WS can also be seen in Fig. 11. Based on Fig. 11, both retrieval methods yielded similar CLW and WV. As discussed below, wind speeds obtained with 1DVAR were a few meters per second higher than those obtained via Eq. (8), especially around 1930–2000 UTC, likely owing to differences in how each method performs its retrievals (i.e., multiple linear regression vs inversion). In addition, some pixels were masked by 1DVAR but unmasked for the new retrieval equations; this may have been caused by regions of supercooled cloud water collocated with snow (i.e., precipitation-size ice crystal aggregates), which are not accounted for in 1DVAR, causing 1DVAR to not reach convergence on a solution for these pixels. However, both methods yielded nearly the same CLW and WV and similar WS across these AMPR scans, including capturing the slantwise WS gradients around 2005–2017 UTC, indicating good agreement and their ability to perform these retrievals. In addition, some minor cross-track stripe artifacts may be seen in Fig. 11

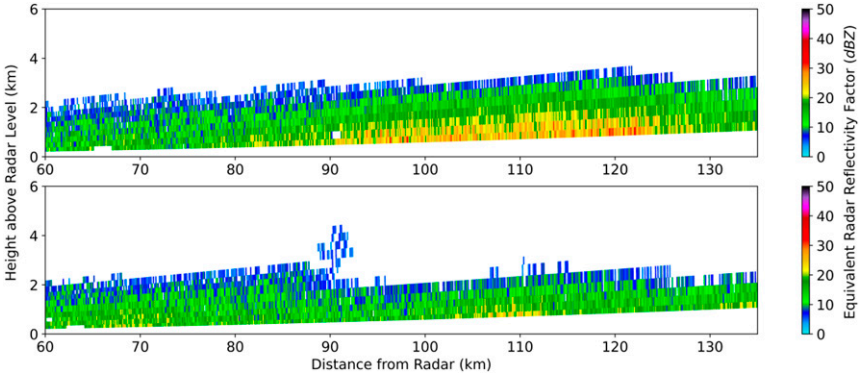

FIG. 10. Range–height indicator (RHI) scans of equivalent radar reflectivity factor (Z_H) measured by the NPOL radar at 2022 UTC 24 Nov 2015. RHI scans along azimuth angles (top) 224° and (bottom) 227°.

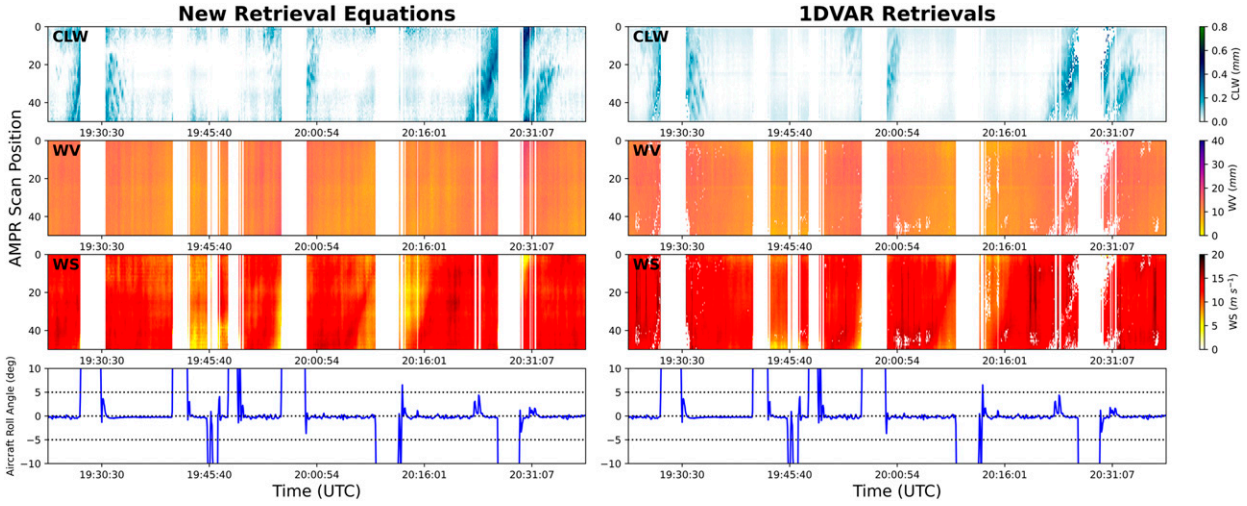

FIG. 11. Values of (top) cloud liquid water, (second from top) water vapor, and (second from bottom) 10-m wind speed calculated using (left) the new geophysical retrieval equations and (right) 1DVAR from the AMPR data on 24 Nov 2015 shown in Fig. 9. (bottom) The ER-2 aircraft roll angle. For CLW retrievals via the new equation, pixels with CLW < 0 mm after applying the T_b bias corrections have been masked.

(and in the next case presented below), but these apparent EIA effects are largely within expected uncertainties at a 95% confidence interval for the new retrieval equations and 1DVAR, as shown in Fig. S1 in the online supplemental material.

To further examine CLW, WV, and WS retrieved using Eqs. (6)–(8) compared to 1DVAR, 2D histograms were made between the two methods for all quality-controlled AMPR pixels on 24 November. These histograms are presented in Fig. 12, where it can be seen that a majority of CLW and WV data points fall near their respective 1-to-1 ratio lines, indicating good agreement. Most WS data points are shifted above the 1-to-1 ratio line, indicating that Eq. (8)'s WS values were generally lower than those calculated via 1DVAR, likely due to use of multiple linear regression rather than inversion. As will be discussed further for the next case, breakpoints along the WS y axis in Fig. 12 (e.g., at 15 m s^{-1}) were also likely caused by pixels where 1DVAR's solution remained close to the a priori value due to the presence of precipitation.

To summarize Eqs. (6)–(8) compared to 1DVAR, RMSD and MedAD values were calculated for all quality-controlled AMPR pixels from the four OLYMPEX/RADEX cases, as seen in Table 2; 24 November had CLW, WV, and WS RMSD values of approximately 3.78×10^{-2} mm, 1.63 mm, and 1.69 m s^{-1}, respectively, and MedAD values of approximately 1.83×10^{-2} mm, 1.03 mm, and 0.76 m s^{-1}, respectively. The relatively low RMSD and MedAD values match the good agreement between the two methods in Fig. 12, especially for CLW. These results indicate that geophysical values calculated via Eqs. (6)–(8) correlate well with 1DVAR, which matches the results of Wentz (1997) and suggests that both methods can be useful in these retrievals.

Next, for comparison with in situ observations, WV and WS calculated via Eqs. (7) and (8) were compared with values calculated using AVAPS dropsondes from the same case dates. As described in section 4, 10-m AVAPS wind speed was calculated using Eqs. (13) or (14) and AVAPS water vapor was calculated using Eq. (15). The differences between AVAPS and AMPR wind speed and water vapor around the time AVAPS reached minimum height and around the time AMPR passed over the AVAPS minimum height location can be found in Fig. 13. From the left plots in Fig. 13, the wind speed difference was less than 1 m s^{-1} for both available dropsondes on 24 November, indicating excellent agreement between AMPR-derived WS and in situ observations. AMPR and AVAPS were approximately 40 and 80 km apart at the minimum height times, so this agreement indicates similar wind speeds at the AMPR and AVAPS locations and lack of isolated convection impacting the WS comparisons, as discussed in the next case. Likewise, the water vapor differences less than 2.5 mm indicate good agreement between AMPR and AVAPS, which is near the highest precision observed by Wilheit and Chang (1980) of 1.5 mm, and matches the fairly uniform water vapor seen in Fig. 11. However, the AMPR–AVAPS spatial offset likely contributed to the differences seen in Fig. 13, which is a limitation of comparing data from instruments on separate aircraft.

From the right plots in Fig. 13, it can be seen further that AVAPS observations agreed very well with AMPR-derived values; wind speed differences were less than 0.5 m s^{-1} when AMPR passed over the AVAPS minimum height location for both 24 November dropsondes. This is most trustworthy for the 1759 UTC dropsonde, since AMPR passed over the minimum height location less than 15 min prior. However, the 0.11 m s^{-1} difference for the 1749 UTC dropsonde is interesting considering the time difference greater than 2.5 h, which was the highest temporal offset in this study. Water vapor agreement was also strong, with differences of approximately 2 mm or less. As previously noted, these good agreements likely resulted in part from the large amount of clear-air data minimizing any contamination from isolated convection. Additionally, despite the presence of a low pressure center off the coast of Oregon at 1800 UTC, surface pressure gradients over the domain were

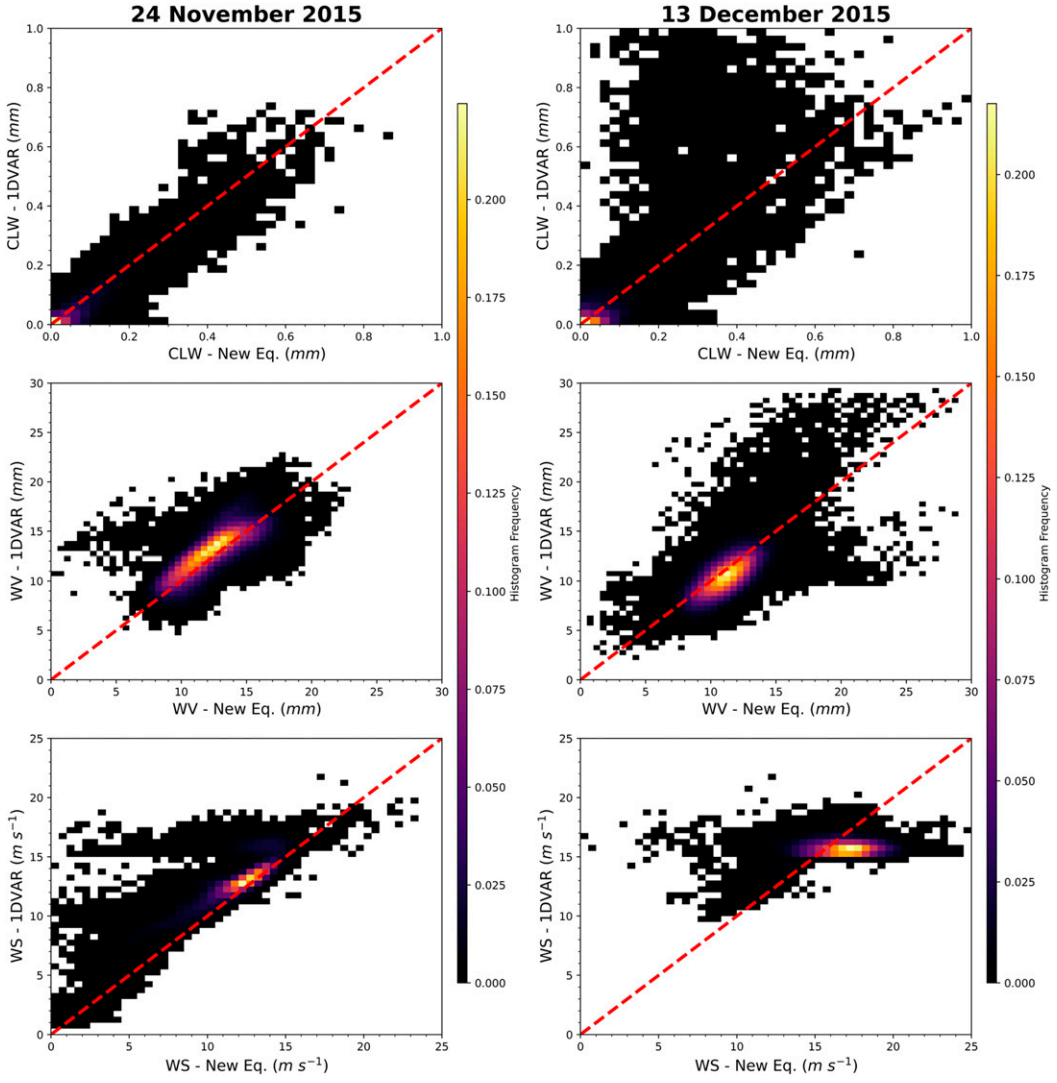

FIG. 12. Two-dimensional histograms comparing (top) cloud liquid water, (middle) water vapor, and (bottom) 10-m wind speed calculated using the new retrieval equations (x axes) and 1DVAR (y axes) for all quality-controlled AMPR pixels during the ER-2 flights on (left) 24 Nov and (right) 13 Dec 2015. The red dashed line in each plot indicates a one-to-one ratio between the two retrieval methods.

relatively low at 1800 UTC (UWYO 2019). This likely contributed to the relatively strong agreements in water vapor and wind speed despite the spatial and temporal offsets, especially for the 2.5-h offset for the 1749 UTC dropsonde.

b. *Case 2: 13 December 2015*

During the 13 December 2015 case, similar to 24 November, a relatively high-amplitude, positively tilted trough propagated through the study region; however, the low pressure center was deeper for 13 December, with 1000-hPa geopotential heights as low as −90 m at 1200 UTC (UWYO 2019). Horizontally polarized deconvolved T_b during part of the ER-2 flight can be found in Fig. 9, where scattered convection is indicated by local maxima in T_b throughout the flight path. This contrasts the light precipitation on 24 November and allowed for the retrievals to be tested within stronger convection.

CLW, WV, and WS retrieved using Eqs. (6)–(8) and the 13 December data in Fig. 9 are presented in Fig. 14, where the T_b maxima are reflected by local CLW and WV maxima. The 13 December WS pattern was more complex than 24 November, indicated by local WS maxima up to 20 m s^{-1}; the higher mean background wind on 13 December compared to 24 November may have resulted from the more intense low pressure center and associated slightly higher pressure gradient on 13 December and the passage of a cold front on this day [Weather Prediction Center (WPC); WPC 2019]. The slight bow-like appearance to some local WS maxima (e.g., around 1940 UTC) is interesting. Given the location of this WS maximum near the local CLW and WV maxima, it is possible that

TABLE 2. An overview of the median RMSD values between 1DVAR and the new retrieval equations for CLW, WV, and WS (second through fourth columns, respectively) during each of the four OLYMPEX/RADEX case dates analyzed in this study, as well as the median MedAD values between these retrieval methods for CLW, WV, and WS (fifth through seventh columns, respectively) and the correlation coefficient (CC) values between the two retrieval methods for CLW, WV, and WS (eighth through tenth columns, respectively). The median value for each statistic calculated across the four case dates is presented in the bottom row. All values were calculated across all quality-controlled AMPR data for each case.

Date	CLW RMSD (mm)	WV RMSD (mm)	WS RMSD (m s^{-1})	CLW MedAD (mm)	WV MedAD (mm)	WS MedAD (m s^{-1})	CLW CC	WV CC	WS CC
23 Nov 2015	1.01×10^{-1}	2.47	2.64	2.72×10^{-2}	1.40	2.13	0.76	0.50	0.85
24 Nov 2015	3.78×10^{-2}	1.63	1.69	1.83×10^{-2}	1.03	0.76	0.89	0.77	0.86
10 Dec 2015	2.55×10^{-1}	2.26	4.68	5.67×10^{-2}	1.26	4.12	0.76	0.81	−0.27
13 Dec 2015	9.81×10^{-2}	1.73	2.06	3.03×10^{-2}	1.02	1.51	0.76	0.66	0.23
Median	9.95×10^{-2}	2.00	2.35	2.88×10^{-2}	1.14	1.82	0.76	0.72	0.54

this feature, as well as other small-scale WS variability, is a gust front associated with a convective storm. This is noteworthy as it indicates the potential to estimate gust-front wind speeds using AMPR data and Eq. (8).

To demonstrate that these high-WS areas are not strictly due to rain impact on the AMPR signal, CLW data were masked for CLW > 0.01 mm, as seen in Fig. 15. Since the WS maxima fall outside areas where CLW is greater than 0.01 mm, they avoid potential rain contamination. Although all AMPR data are sampled at a 0.6-km cross-track resolution, the raw resolution of the 10.7- and 19.35-GHz data is 2.8 km. To avoid potential influences of CLW on WS estimations (e.g., O'Dell et al. 2008), all WS data within ±5 pixels, or roughly 3 km, of a CLW > 0.01 mm observation were masked in the along-track and across-track dimensions. These results are presented in the second panel of Fig. 15, where it can be seen that WS maxima fall outside of these potentially cloud-affected pixels, further suggesting that these WS signatures are not the result of a data artifact. In addition, NPOL RHIs through convective storms around the same time as these AMPR analyses are presented in Fig. 16, wherein the radial velocity (V_r) values within the precipitating storms stand out against the background wind field and support the inference of gust fronts. Gust-front analysis with AMPR data needs further examination in future work, but the potential exists for these analyses to be performed.

Retrieved CLW, WV, and WS via 1DVAR on 13 December are also shown in Fig. 14, where it can be seen that 1DVAR did not yield output for several pixels where T_b values were relatively high. The precipitation implied by these high T_b values,

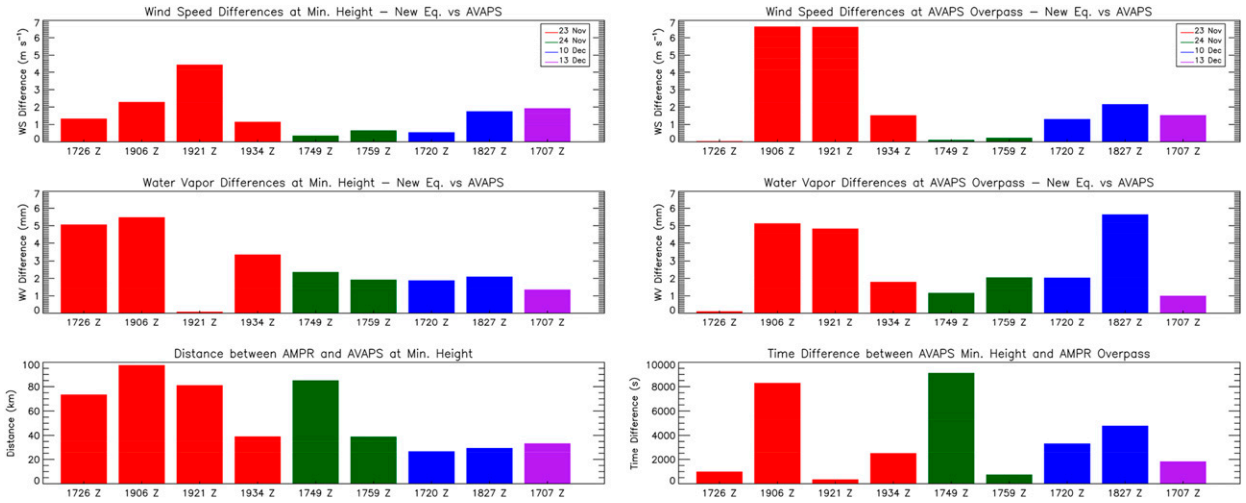

FIG. 13. Absolute values of the differences between (top) 10-m wind speed calculated using the new retrieval equations and calculated from AVAPS data for the four case study dates: 23 Nov (red bars), 24 Nov (green bars), 10 Dec (blue bars), and 13 Dec 2015 (purple bars). (middle) Absolute values of the differences between water vapor via the same calculations. These calculations were performed at two times: (left) at the time the AVAPS dropsonde reached its minimum recorded height and (right) at the time AMPR passed over the location where AVAPS recorded its minimum height. (bottom left) Spatial offsets between AMPR and AVAPS at the time AVAPS reached its minimum recorded height. (bottom right) Temporal offsets between when AVAPS reached its minimum recorded height and when AMPR passed over the location where AVAPS recorded its minimum height; these spatial and temporal offsets are based on the values seen in Table 1. The *x* axis in each plot represents the launch times of the respective AVAPS dropsondes. Wind speed and water vapor values calculated using AMPR data were averaged over a time period of approximately 10 min, as described in the main text.

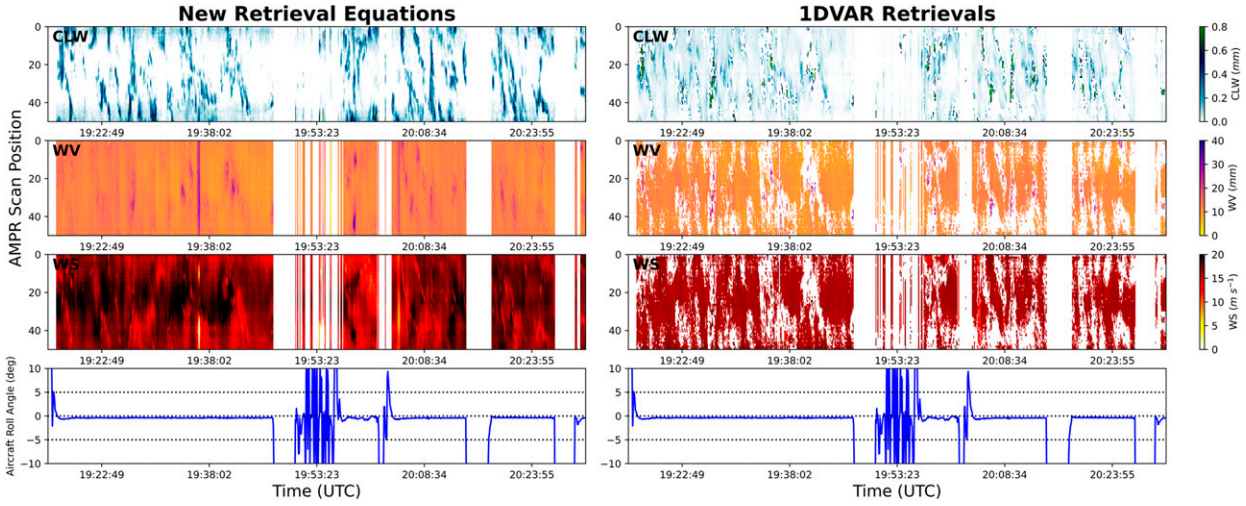

FIG. 14. As in Fig. 11, but for a portion of the ER-2 flight on 13 Dec 2015.

especially at 10.7 and 19.35 GHz, is not accounted for in 1DVAR's forward model; 1DVAR's cost function increased nearer the T_b maxima (not shown), and eventually 1DVAR failed to reach a solution within these T_b maxima. This resulted in 1DVAR's WS reverting back to the GEOS-5 a priori throughout Fig. 14, especially near the T_b maxima, which, as seen in Fig. 12 and discussed below, resulted in 1DVAR not capturing the smaller-scale WS variability that was captured by Eq. (8). However, background wind speed was similar between the two methods. Mean WV was also similar between 1DVAR and Eq. (7), and local CLW maxima were captured by both methods.

These results indicate fair agreement between both methods, but to further examine the correlation between 1DVAR and Eqs. (6)–(8), 2D histograms across all quality-controlled AMPR pixels on 13 December are shown in Fig. 12. From Fig. 12, the methods agreed well for CLW and WV for most pixels; however, the WS pattern is interesting. WS less than 15 m s^{-1} saw similar behavior as on 24 November, where Eq. (8) yielded values a few m s^{-1} less than 1DVAR; however, for WS greater than the artifact around 15 m s^{-1} on the y axis, Eq. (8) yielded higher WS (by 10 m s^{-1} in some cases) for many pixels. This is reflected in a low correlation coefficient of 0.23 between Eq. (8) and 1DVAR WS on 13 December, shown in Table 2. A significant reason for this difference arises from Eq. (8) attempting to retrieve even in pixels where precipitation is present, whereas 1DVAR typically fails to reach convergence in these pixels and will revert back to its a priori value in nearby pixels. Wind speeds in the GEOS-5 data nearest the 13 December 2015 flight path were around 15–18 m s^{-1} (not shown). Thus, in pixels where 1DVAR reverted back to its background values on this day (e.g., around precipitation), the wind speed values output from 1DVAR were around 15–18 m s^{-1}, which seemed to yield the high data concentration around these values on the y axis in Fig. 12. The retrievals attempted by Eq. (8) near precipitation regions likely contributed to its higher WS compared to 1DVAR in Fig. 12, in addition to any differences resulting from use of multiple linear regression versus 1DVAR's inversion method.

To evaluate other sources that may contribute to the breakpoint and data clustering around 15 m s^{-1}, we performed several analyses using pixels where 1DVAR reached convergence (not shown) targeting three hypotheses for this behavior: 1) 1DVAR encountered difficulties calculating WS near nadir due to little difference in the horizontally and vertically polarized T_b data; 2) high CLW values (i.e., near, but largely not within, precipitation) also caused 1DVAR to revert back to the GEOS-5 a priori wind speeds; and 3) 1DVAR reached convergence on WS values that were different from the a priori value, but with a cost function (χ^2) value that was unacceptably large (i.e., $\chi^2 > 10$; Duncan and Kummerow 2016), causing 1DVAR to use the a priori wind speeds. For each of these analyses, different levels of masking were individually applied to the retrieved WS from 1DVAR and Eq. (8); all data with EIA $< 10°$, 20°, 30°, and 40° were masked, as were all pixels with retrieved CLW $> 1 \times 10^{-4}$, 5×10^{-4}, 1×10^{-3}, and 5×10^{-3} mm, and all pixels with a 1DVAR χ^2 value > 0.5, 1, 5, and 10. In all cases, the data clustering around 15–18 m s^{-1} on the 1DVAR axis persisted, as did the 15 m s^{-1} breakpoint. However, as fewer and fewer pixels nearer the middle of the scan swath were considered via the increased EIA masking levels, the WS data points converged on the 1-to-1 ratio line between the two retrieval methods, indicating greater agreement between the methods, despite the continued breakpoint. The same phenomenon was observed when applying χ^2 masks, with data points converging on the 1-to-1 ratio line more strongly when masking $\chi^2 > 0.5$ compared to $\chi^2 > 10$. This convergence was not observed for the different levels of CLW masking. Thus, while masking the AMPR data based on EIA and 1DVAR's χ^2 value indicated improved agreement between the retrieval methods, they did not fully explain the 15 m s^{-1} breakpoint along 1DVAR's axis or the clustering of 1DVAR WS around 15–18 m s^{-1}. This is especially interesting for the increased χ^2 values, as it indicates that, while precipitation influenced 1DVAR's retrievals, the increases in χ^2 nearer precipitation did not seem to fully explain the 15 m s^{-1} breakpoint.

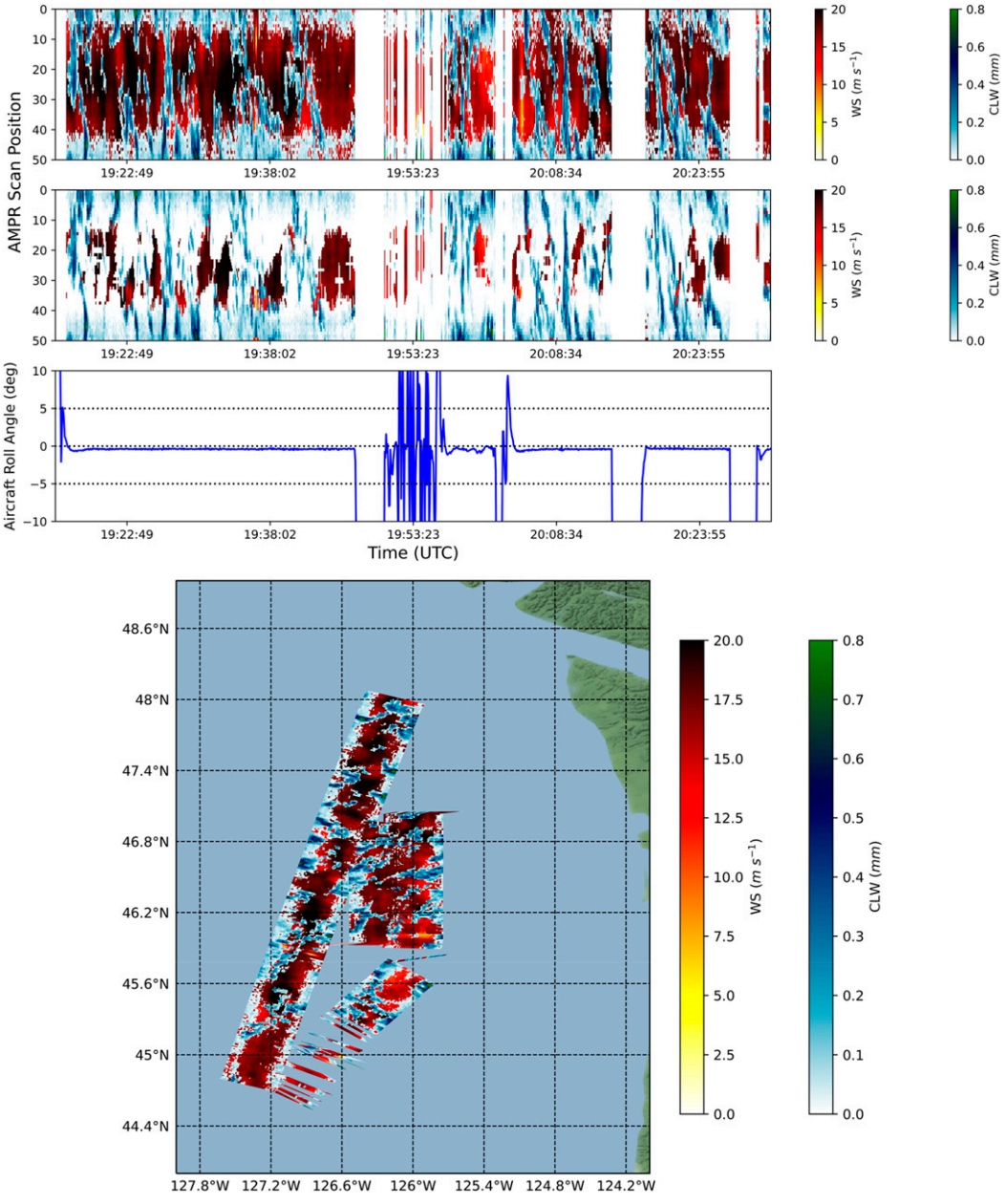

FIG. 15. (top) A plot of 10-m wind speeds for AMPR pixels where the cloud liquid water was ≤0.01 mm (red color bar) and cloud liquid water values for AMPR pixels where the cloud liquid water was >0.01 mm (blue color bar) during the portion of the 13 Dec 2015 ER-2 flight shown in Fig. 14. (bottom) As in the top panel, except presented in a geolocated manner. (second from top) Cloud liquid water values (blue color bar) for all pixels within ±5 pixels in the cross-track or along-track directions of any pixel with a cloud liquid water value >0.01 mm, with wind speed values (red color bar) plotted for all pixels that did not meet these criteria. (third from top) ER-2 aircraft roll angle over the same time period.

Apart from this WS behavior, Eqs. (6)–(8) and 1DVAR agreed fairly well. This is further reflected in the CLW, WV, and WS RMSD values of 9.81×10^{-2} mm, 1.73 mm, and 2.06 m s^{-1}, respectively, in Table 2 and MedAD values of 3.03×10^{-2} mm, 1.02 mm, and 1.51 m s^{-1}, respectively. These values agree with the deviations from the 1-to-1 ratio line in Fig. 12 and indicate fairly good agreement between the retrieval methods.

To compare AMPR-derived WV and WS with in situ observations on 13 December, an AVAPS data analysis similar to 24 November was performed. However, only one dropsonde was available during the ER-2 flight on 13 December.

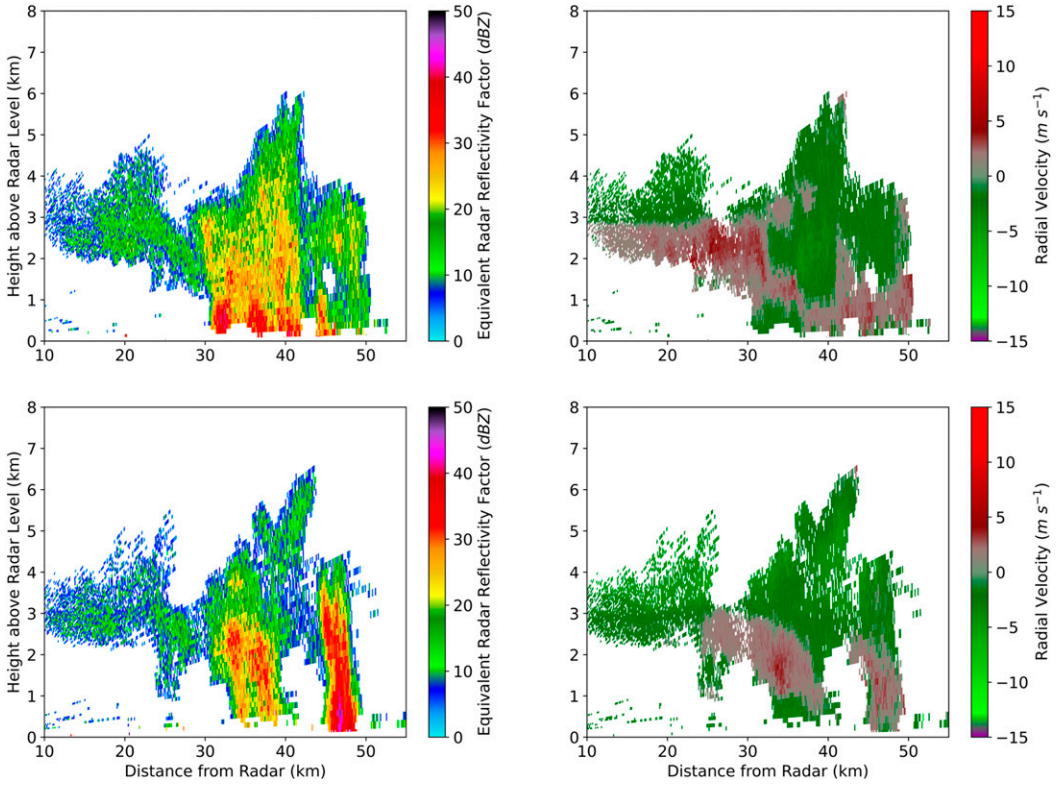

FIG. 16. Range–height indicator (RHI) scans of (top left) equivalent radar reflectivity factor (Z_H) and (top right) radial velocity (V_r) measured by the NPOL radar at 1920 UTC 13 Dec 2015 along an azimuth angle of 210°. (bottom) As in the top panels, but measured along an RHI azimuth angle of 216°.

Comparing AVAPS and AMPR at the time of AVAPS minimum height, seen in Fig. 13, the wind speed and water vapor differences were roughly 1.93 m s^{-1} and 1.36 mm, respectively, which is good agreement despite AMPR being more than 30 km from AVAPS. Examining AMPR's overpass of the AVAPS minimum height location, which took place 30 min later as seen in Fig. 13, the wind speed and water vapor differences were about 1.54 m s^{-1} and 1.01 mm, respectively, which is very good agreement with a relatively low temporal offset. In general, WV and WS from Eqs. (7) and (8) compared well with AVAPS on 13 December, which likely resulted from surface pressure gradients that were only slightly greater than those on 24 November (UWYO 2019).

c. *Summary of all case dates*

The overall performances of Eqs. (6)–(8) compared to 1DVAR are indicated by the RMSD and MedAD values in Table 2. The median MedAD values calculated across the four cases were 2.88×10^{-2} mm, 1.14 mm, and 1.82 m s^{-1} for CLW, WV, and WS, respectively, while median RMSD values were 9.95×10^{-2} mm, 2.00 mm, and 2.35 m s^{-1}, respectively. These results indicate excellent agreement between the new retrieval equations and 1DVAR overall. CLW yielded the lowest uncertainty of all three parameters, as in Wentz (1997), with RMSD and MedAD values on the same order of magnitude as observed in Wentz (1997) and Wilheit and Chang (1980). The WV RMSD of 2.0 mm is approximately 0.6 mm lower than that noted in Duncan and Kummerow (2016), but is approximately 0.8 mm higher than the RMSD noted in Wentz (1997). In addition, the overall WS MedAD of 1.82 m s^{-1} is 0.18 m s^{-1} below the baseline uncertainty of 2.0 m s^{-1} noted in past wind retrieval studies (e.g., Wentz and Meissner 2007; Ruf et al. 2019), while the WS RMSD of 2.35 m s^{-1} falls slightly above this baseline uncertainty. However, WS RMSD increased due to use of a one-step retrieval equation compared to the two-step approach used in past studies, such as the RMSD of 1.0–1.8 m s^{-1} noted in Wilheit and Chang (1980). These factors indicate improvements in geophysical retrievals that are possible with these new equations when applied to AMPR data. A notable feature in Table 2 is the relatively high MedAD and RMSD values for WS on 10 December, which are nearly double the second-highest values. As with 13 December, a high amount of precipitation was present on 10 December, which impacted the retrievals due to the differences in how both methods handle precipitation.

The overall performance of Eqs. (7) and (8) compared to AVAPS can be found in Fig. 13. The MedAD for WV and WS calculated across all nine dropsondes was 2.10 mm and 1.15 m s^{-1}, respectively, at the time AVAPS reached minimum height, while MedAD at the location of AVAPS minimum height was 1.80 mm and 1.53 m s^{-1}, respectively. Cases where AMPR-derived and AVAPS-derived WV and WS differed

considerably (e.g., 1906 and 1921 UTC 23 November) were influenced by isolated convection (not shown); in some cases, AMPR was over an isolated convective storm while AVAPS was dropped away from the storm, thus impacting WV and WS comparisons at AVAPS minimum height time. Similarly, in some cases (including the two aforementioned 23 November dropsondes), a convective storm developed around the AVAPS minimum height location during the time between AVAPS reaching minimum height and the ER-2 passing over that location.

Furthermore, a cold front extended through the center of the study domain at 1800 UTC 23 November (UWYO 2019), which likely contributed to the considerable differences in the dropsondes around 1900 UTC on this day. The surface pressure gradients were relatively low away from the cold front on 23 November, which may have contributed to relatively good agreements in the 1726 and 1934 UTC dropsondes. Conversely, pressure gradients were significantly higher on 10 December in association with an intense low pressure center northwest of Washington (UWYO 2019), which likely contributed to the differences seen over time for the 1827 UTC dropsonde in Fig. 13. This suggests that dropsondes with a relatively high spatial and/or temporal offset on 23 November and 10 December, such as those at 1726, 1906, and 1921 UTC 23 November and 1827 UTC 10 December, may present a less-reliable comparison for water vapor and wind speed validations compared to those with a high spatial and/or temporal offset on 24 November and 13 December. Therefore, the 1934 UTC dropsonde on 23 November and the 1720 UTC dropsonde on 10 December present the most reliable comparisons for these two case dates. These are example limitations of comparing data from instruments flown on different aircraft.

Despite these temporal and spatial offset issues, both sets of MedAD indicate that WV and WS from Eqs. (7) and (8) agreed fairly strongly with AVAPS. Both WS MedAD values are less than the 2.0 m s^{-1} baseline uncertainty noted in Wentz and Meissner (2007) and Ruf et al. (2019), and are similar to the WS RMSD of 1.2 and 0.9 m s^{-1} reported in Duncan and Kummerow (2016) and Wentz (1997), respectively. Likewise, the WV MedAD values are 0.5–0.8 mm lower than the 2.6-mm RMSD noted in Duncan and Kummerow (2016), but are 0.6–0.9 mm higher than the 1.2-mm RMSD presented in Wentz (1997).

6. Summary and future work

The purpose of this manuscript was to provide an overview of AMPR's polarimetric upgrades and calibrations, and to demonstrate the ability to obtain realistic CLW, WV, and WS from AMPR data via three new geophysical retrieval equations. AMPR T_b simulated from NCEP GDAS atmospheric profiles were used to train the retrieval equations, and their performances were initially tested against geophysical data from the GDAS profiles. The new retrieval equations were then applied to AMPR T_b recorded during four OLYMPEX/RADEX cases, the results of which were compared to the same parameters calculated via 1DVAR for the same AMPR dataset. Mixed-polarization AMPR T_b were deconvolved into true horizontally and vertically polarized T_b, and biases in observed T_b were removed prior to using the new equations with OLYMPEX/RADEX data. WV and WS calculated via the new retrieval equations were also compared with in situ AVAPS dropsonde data.

Comparing retrievals from simulated AMPR T_b against the GDAS profiles yielded nearly unbiased mean CLW retrieval error across the range of CLW values examined, with minimal crosstalk errors apart from WV greater than 30 mm. Mean WV retrieval error was near 0 mm for WV less than 50 mm, and crosstalk errors were around 0 mm. Retrieval error for WS fluctuated from negative values for WS less than 5 and greater than 15 m s^{-1} to positive values for WS between 5 and 15 m s^{-1}, though mean error magnitude was less than 1 m s^{-1} for WS between 3 and 19 m s^{-1}. WS crosstalk errors were nearly unbiased apart from SST between 0° and 3°C, where the mean error magnitude was still less than 1 m s^{-1}. Mean retrieval RMSD for CLW, WV, and WS were 0.11 mm, 1.28 mm, and 1.11 m s^{-1}, respectively, while the respective median MedAD values were 2.26×10^{-2} mm, 0.22 mm, and 0.55 m s^{-1}.

Using AMPR T_b data collected during OLYMPEX/RADEX to calculate the geophysical parameters, there was relatively strong agreement between the new equations and 1DVAR. Both methods were able to retrieve similar values in clear air, while the new equations attempted to retrieve in light precipitation on 24 November and in stronger convection on 13 December, whereas 1DVAR does not converge on a solution in precipitation regions, leading to differences in the retrievals around areas of precipitation. The new WS equation captured small-scale WS variability on 13 December that may have been associated with gust fronts, which demonstrates its utility in analyzing smaller-scale features. Median RMSD for CLW, WV, and WS across the four cases was 9.95×10^{-2} mm, 2.00 mm, and 2.35 m s^{-1}, respectively, while median MedAD was 2.88×10^{-2} mm, 1.14 mm, and 1.82 m s^{-1}, respectively.

When comparing WV and WS from the new equations with AVAPS, two approaches were taken: 1) compare both datasets at the time of AVAPS minimum height, regardless of spatial offset, and 2) compare both datasets at the location of AVAPS minimum height, regardless of temporal offset. For the nine available dropsondes, the WV MedAD was 2.10 and 1.80 mm at the time and location of AVAPS minimum height, respectively, while the respective WS MedAD values were 1.15 and 1.53 m s^{-1}. These results indicate that the new WV and WS equations compared well with in situ observations, despite the spatial and temporal offsets between the instruments and associated errors resulting from isolated convection and pressure gradients.

The results herein are promising, but future work must further analyze the new retrieval equations. One avenue for future work could expand the analysis of WS artifacts observed in some of the 1DVAR data to consider other error sources. Training an artificial neural network to perform the geophysical retrievals would be interesting, given the potential for deviations in the multiple-linear regression equations where the assumed relation between the retrieved property and the

T_b values does not wholly represent their true relation. Additional OLYMPEX/RADEX cases should be tested and compared with the results herein, which will be performed as the entire OLYMPEX/RADEX dataset is reprocessed using Eqs. (6)–(8). Comparing CLW with in situ data may be challenging, but would provide useful validation. Testing the equations on AMPR datasets from other field campaigns, such as the recent Cloud, Aerosol and Monsoon Processes Philippines Experiment (CAMP^{2}Ex), where AMPR and AVAPS were flown on the same aircraft, and Investigation of Microphysics and Precipitation for Atlantic Coast-Threatening Snowstorms (IMPACTS), will also be beneficial to examine their performances in other climate regions throughout the world.

Acknowledgments. The authors thank Jack Kaye, Hal Maring, and Ramesh Kakar at NASA Headquarters for their financial support of AMPR deployments and data analysis, and the first author would like to acknowledge research support from NASA Marshall Space Flight Center (MSFC) through Cooperative Agreement NNM11AA01A between NASA MSFC and The University of Alabama in Huntsville (UAH). We acknowledge Anthony Guillory (NASA), Eric Cantrell (NASA), Kurt Dietz (NASA), Dave Simmons (UAH), and Karthik Srinivasan (NASA) for their project management and engineering support during the OLYMPEX/RADEX field campaign, as well as Brent Roberts (NASA) and Paul Meyer (NASA) for their assistance with OLYMPEX/RADEX data processing and quality control. Furthermore, we thank the three anonymous reviewers for their thoughtful comments and suggestions, which helped improve the quality of this manuscript. The first author would also like to thank Larry Carey (UAH) for providing computer resources and helpful feedback to support his work on this study.

REFERENCES

Amarin, R. A., W. L. Jones, S. F. El-Nimri, J. W. Johnson, C. S. Ruf, T. L. Miller, and E. Uhlhorn, 2012: Hurricane wind speed measurements in rainy conditions using the airborne Hurricane Imaging Radiometer (HIRAD). *IEEE Trans. Geosci. Remote Sens.*, **50**, 180–192, https://doi.org/10.1109/TGRS.2011.2161637.

American Meteorological Society, 2019: Precipitable water. Glossary of Meteorology, http://glossary.ametsoc.org/wiki/Precipitable_water.

Berg, W., M. R. P. Sapiano, J. Horsman, and C. Kummerow, 2013: Improved geolocation and Earth incidence angle information for a fundamental climate data record of the SSM/I sensors. *IEEE Trans. Geosci. Remote Sens.*, **51**, 1504–1513, https://doi.org/10.1109/TGRS.2012.2199761.

Bhargava, K., E. Kalnay, J. A. Carton, and F. Yang, 2018: Estimation of systematic errors in the GFS using analysis increments. *J. Geophys. Res. Atmos.*, **123**, 1626–1637, https://doi.org/10.1002/2017JD027423.

Biswas, S. K., S. Farrar, K. Gopalan, A. Santos-Garcia, W. L. Jones, and S. Bilanow, 2013: Intercalibration of microwave radiometer brightness temperatures for the Global Precipitation Measurement Mission. *IEEE Trans. Geosci. Remote Sens.*, **51**, 1465–1477, https://doi.org/10.1109/TGRS.2012.2217148.

——, T. J. Lang, D. Duncan, and C. Kummerow, 2017: Polarization deconvolution and geophysical retrieval from a dual-pol, cross-track scanning microwave radiometer (AMPR) during OLYMPEX/RADEX. *2017 Fall Meeting*, New Orleans, LA, Amer. Geophys. Union, Abstract H32C-07.

Bowman, K. P., C. R. Homeyer, and D. G. Stone, 2009: A comparison of oceanic precipitation estimates in the tropics and subtropics. *J. Appl. Meteor. Climatol.*, **48**, 1335–1344, https://doi.org/10.1175/2009JAMC2149.1.

Cecil, D. J., and S. K. Biswas, 2017: Hurricane Imaging Radiometer (HIRAD) wind speed retrievals and validation using dropsondes. *J. Atmos. Oceanic Technol.*, **34**, 1837–1851, https://doi.org/10.1175/JTECH-D-17-0031.1.

——, K. R. Quinlan, and D. M. Mach, 2010: Intense convection observed by NASA ER-2 in Hurricane Emily (2005). *Mon. Wea. Rev.*, **138**, 765–780, https://doi.org/10.1175/2009MWR3063.1.

Duncan, D. I., and C. D. Kummerow, 2016: A 1DVAR retrieval applied to GMI: Algorithm description, validation, and sensitivities. *J. Geophys. Res. Atmos.*, **121**, 7415–7429, https://doi.org/10.1002/2016JD024808.

Evans, K. F., J. Turk, T. Wong, and G. L. Stephens, 1995: A Bayesian approach to microwave precipitation profile retrieval. *J. Appl. Meteor.*, **34**, 260–279, https://doi.org/10.1175/1520-0450-34.1.260.

Helmus, J. J., and S. M. Collis, 2016: The Python ARM Radar Toolkit (Py-ART), a library for working with weather radar data in the Python programming language. *J. Open Res. Software*, **4**, e25, https://doi.org/10.5334/jors.119.

Hock, T., and K. Young, 2017: GPM ground validation Advanced Vertical Atmospheric Profiling System (AVAPS) OLYMPEX. NASA Global Hydrology Resource Center DAAC, accessed 13 June 2019, https://doi.org/10.5067/GPMGV/OLYMPEX/AVAPS/DATA101.

Hong, S., and I. Shin, 2013: Wind speed retrieval based on sea surface roughness measurements from spaceborne microwave radiometers. *J. Appl. Meteor. Climatol.*, **52**, 507–516, https://doi.org/10.1175/JAMC-D-11-0209.1.

Houze, R. A., Jr., and Coauthors, 2017: The Olympic Mountains Experiment (OLYMPEX). *Bull. Amer. Meteor. Soc.*, **98**, 2167–2188, https://doi.org/10.1175/BAMS-D-16-0182.1.

Kummerow, C., W. S. Olson, and L. Giglio, 1996: A simplified scheme for obtaining precipitation and vertical hydrometeor profiles from passive microwave sensors. *IEEE Trans. Geosci. Remote Sens.*, **34**, 1213–1232, https://doi.org/10.1109/36.536538.

Leppert, K. D., and D. J. Cecil, 2015: Signatures of hydrometeor species from airborne passive microwave data for frequencies 10–183 GHz. *J. Appl. Meteor. Climatol.*, **54**, 1313–1334, https://doi.org/10.1175/JAMC-D-14-0145.1.

Liebe, H. J., 1985: An updated model for millimeter wave propagation in moist air. *Radio Sci.*, **20**, 1069–1089, https://doi.org/10.1029/RS020i005p01069.

——, 1989: MPM—An atmospheric millimeter-wave propagation model. *Int. J. Infrared Millimeter Waves*, **10**, 631–650, https://doi.org/10.1007/BF01009565.

——, G. A. Hufford, and T. Manabe, 1991: A model for the complex permittivity of water at frequencies below 1 THz. *Int. J. Infrared Millimeter Waves*, **12**, 659–675, https://doi.org/10.1007/BF01008897.

McGaughey, G., E. J. Zipser, R. W. Spencer, and R. E. Hood, 1996: High-resolution passive microwave observations of convective systems over the tropical Pacific Ocean. *J. Appl. Meteor.*, **35**, 1921–1947, https://doi.org/10.1175/1520-0450(1996)035<1921:HRPMOO>2.0.CO;2.

Meissner, T., and F. J. Wentz, 2012: The emissivity of the ocean surface between 6 and 90 GHz over a large range of wind speeds and Earth incidence angles. *IEEE Trans. Geosci. Remote Sens.*, **50**, 3004–3026, https://doi.org/10.1109/TGRS.2011.2179662.

Mie, G., 1908: Beiträge zur Optik trüber Medien, speziell kolloidaler Metallösungen. *Ann. Phys.*, **330**, 377–445, https://doi.org/10.1002/ANDP.19083300302.

NCEP, 2000: NCEP FNL operational model global tropospheric analyses, continuing from July 1999. National Center for Atmospheric Research Computational and Information Systems Laboratory, accessed 3 April 2017, https://doi.org/10.5065/D6M043C6.

O'Dell, C. W., F. J. Wentz, and R. Bennartz, 2008: Cloud liquid water path from satellite-based passive microwave observations: A new climatology over the global oceans. *J. Climate*, **21**, 1721–1739, https://doi.org/10.1175/2007JCLI1958.1.

Piepmeier, J. R., D. G. Long, and E. G. Njoku, 2008: Stokes antenna temperatures. *IEEE Trans. Geosci. Remote Sens.*, **46**, 516–527, https://doi.org/10.1109/TGRS.2007.909597.

Rodgers, C. D., 2000: *Inverse Methods for Atmospheric Sounding: Theory and Practice*. World Scientific, 238 pp.

Rosenkranz, P. W., 1993: Absorption of microwaves by atmospheric gases. *Atmospheric Remote Sensing by Microwave Radiometry*, M. A. Janssen, Ed., Wiley Series in Remote Sensing and Image Processing, Vol. 6, John Wiley and Sons, 37–90.

——, 1998: Water vapor microwave continuum absorption: A comparison of measurements and models. *Radio Sci.*, **33**, 919–928, https://doi.org/10.1029/98RS01182.

Ruf, C., S. Asharaf, R. Balasubramaniam, S. Gleason, T. Lang, D. McKague, D. Twigg, and D. Waliser, 2019: In-orbit performance of the constellation of CYGNSS hurricane satellites. *Bull. Amer. Meteor. Soc.*, **100**, 2009–2023, https://doi.org/10.1175/BAMS-D-18-0337.1.

Schulte, R. M., and C. D. Kummerow, 2019: An optimal estimation retrieval algorithm for microwave humidity sounding channels with minimal scan position bias. *J. Atmos. Oceanic Technol.*, **36**, 409–425, https://doi.org/10.1175/JTECH-D-18-0133.1.

——, ——, W. Berg, S. C. Reising, S. T. Brown, T. C. Gaier, B. H. Lim, and S. Padmanabhan, 2020: A passive microwave retrieval algorithm with minimal view-angle bias: Application to the TEMPEST-D CubeSat mission. *J. Atmos. Oceanic Technol.*, **37**, 197–210, https://doi.org/10.1175/JTECH-D-19-0163.1.

Shin, D.-B., and C. Kummerow, 2003: Parametric rainfall retrieval algorithms for passive microwave radiometers. *J. Appl. Meteor.*, **42**, 1480–1496, https://doi.org/10.1175/1520-0450(2003)042<1480:PRRAFP>2.0.CO;2.

Smith, E. A., X. Xiang, A. Mugnai, R. E. Hood, and R. W. Spencer, 1994: Behavior of an inversion-based precipitation retrieval algorithm with high-resolution AMPR measurements including a low-frequency 10.7-GHz channel. *J. Atmos. Oceanic Technol.*, **11**, 858–873, https://doi.org/10.1175/1520-0426(1994)011<0858:BOAIBP>2.0.CO;2.

Spencer, R. W., R. E. Hood, F. J. Lafontaine, E. A. Smith, R. Platt, J. Galliano, V. L. Griffin, and E. Lobl, 1994: High-resolution imaging of rain systems with the Advanced Microwave Precipitation Radiometer. *J. Atmos. Oceanic Technol.*, **11**, 849–857, https://doi.org/10.1175/1520-0426(1994)011<0849:HRIORS>2.0.CO;2.

Stephens, G. L., 1990: On the relationship between water vapor over the oceans and sea surface temperature. *J. Climate*, **3**, 634–645, https://doi.org/10.1175/1520-0442(1990)003<0634:OTRBWV>2.0.CO;2.

Straka, J. M., D. S. Zrnić, and A. V. Ryzhkov, 2000: Bulk hydrometeor classification and quantification using polarimetric radar data: Synthesis of relations. *J. Appl. Meteor.*, **39**, 1341–1372, https://doi.org/10.1175/1520-0450(2000)039<1341:BHCAQU>2.0.CO;2.

Uhlhorn, E. W., P. G. Black, J. L. Franklin, M. Goodberlet, J. Carswell, and A. S. Goldstein, 2007: Hurricane surface wind measurements from an operational stepped frequency microwave radiometer. *Mon. Wea. Rev.*, **135**, 3070–3085, https://doi.org/10.1175/MWR3454.1.

UWYO, 2019: Upper air maps. Accessed 22 April 2019, https://weather.uwyo.edu/upperair/uamap.shtml.

Vivekanandan, J., J. Turk, and V. N. Bringi, 1993: Comparisons of precipitation measurements by the advanced microwave precipitation radiometer and multiparameter radar. *IEEE Trans. Geosci. Remote Sens.*, **31**, 860–870, https://doi.org/10.1109/36.239909.

Weng, F., L. Zhao, R. R. Ferraro, G. Poe, X. Li, and N. C. Grody, 2003: Advanced Microwave Sounding Unit cloud and precipitation algorithms. *Radio Sci.*, **38**, 8068, https://doi.org/10.1029/2002RS002679.

Wentz, F. J., 1997: A well-calibrated ocean algorithm for special sensor microwave/imager. *J. Geophys. Res.*, **102**, 8703–8718, https://doi.org/10.1029/96JC01751.

——, and R. W. Spencer, 1998: SSM/I rain retrievals within a unified all-weather ocean algorithm. *J. Atmos. Sci.*, **55**, 1613–1627, https://doi.org/10.1175/1520-0469(1998)055<1613:SIRRWA>2.0.CO;2.

——, and T. Meissner, 2000: Algorithm theoretical basis document (ATBD), version 2: AMSR ocean algorithm. Remote Sensing Systems Tech. Proposal 121599A-1, 67 pp., https://eospso.gsfc.nasa.gov/sites/default/files/atbd/atbd-amsr-ocean.pdf.

——, and ——, 2007: Supplement 1: Algorithm theoretical basis document for AMSR-E ocean algorithms. Remote Sensing Systems Tech. Rep. 051707, 6 pp., http://images.remss.com/papers/amsr/AMSR_Ocean_Algorithm_Version_2_Supplement_1.pdf.

Wilheit, T. T., and A. T. C. Chang, 1980: An algorithm for retrieval of ocean surface and atmospheric parameters from the observations of the scanning multichannel microwave radiometer. *Radio Sci.*, **15**, 525–544, https://doi.org/10.1029/RS015i003p00525.

Wisler, M. M., and J. P. Hollinger, 1977: Estimation of marine environmental parameters using microwave radiometric remote sensing systems. Naval Research Laboratory Memo. Rep. 3661, 27 pp.

Wolff, D., D. A. Marks, W. A. Petersen, and J. Pippit, 2017: GPM Ground Validation NASA S-band dual polarimetric (NPOL) Doppler radar OLYMPEX. NASA Global Hydrology Resource Center DAAC, accessed 8 June 2020, https://doi.org/10.5067/GPMGV/OLYMPEX/NPOL/DATA301.

WPC, 2019: WPC's Surface Analysis Archive. National Weather Service, accessed 23 April 2019, https://www.wpc.ncep.noaa.gov/archives/web_pages/sfc/sfc_archive.php.

Yang, W., H. Meng, R. R. Ferraro, I. Moradi, and C. Devaraj, 2013: Cross-scan asymmetry of AMSU-A window channels: Characterization, correction, and verification. *IEEE Trans. Geosci. Remote Sens.*, **51**, 1514–1530, https://doi.org/10.1109/TGRS.2012.2211884.